Mitochondrial dysfunction-induced KDM5A degradation impairs adult hippocampal neurogenesis in Alzheimer's disease

Dong Kyu Kim
Seoul National University College of Medicine
Hyobin Jeong
EMBL Heidelberg Genome Biology
Jingi Bae
Korea University - Seoul Campus: Korea University
Moon-Yong Cha
LG Chem Ltd Research and Development: LG Chem Ltd Research Park
Moonkyung Kang
Chungnam National University
Dongjin Shin
Seoul National University College of Medicine
Shinwon Ha
DGIST: Daegu Gyeongbuk Institute of Science and Technology
Seung Jae Hyeon
KIST: Korea Institute of Science and Technology
Hokeun Kim
Korea University - Seoul Campus: Korea University
Kyujin Suh
Seoul National University College of Medicine
Mi-Sun Choi
KIT: Korea Institute of Toxicology
Hoon Ryu
KIST: Korea Institute of Science and Technology
Seong-Woon Yu
DGIST: Daegu Gyeongbuk Institute of Science and Technology
Jong-Il Kim
Seoul National University College of Medicine
Yeon-Soo Kim
Chungnam National University
Sang-Won Lee

Korea University - Seoul Campus: Korea University

Daehee Hwang

Seoul National University

Inhee Mook-Jung (inhee@snu.ac.kr)

Seoul National University College of Medicine https://orcid.org/0000-0001-7085-4085

Research article

Keywords: Adult Hippocampal Neurogenesis, Neural Stem Cell, Mitochondria, Epigenetic Regulator, KDM5A, Amyloid Beta, Alzheimer's Disease, Mitochondrial Dysfunction

Posted Date: December 1st, 2020

DOI: https://doi.org/10.21203/rs.3.rs-114597/v1

Abstract

Background Adult hippocampal neurogenesis (AHN) is a process of continuously generating functional mature neurons from neural stem cells in the dentate gyrus. In Alzheimer's disease (AD) brains, amyloid pathology has deleterious effects on AHN, but molecular mechanisms for dysregulated AHN are unclear. Mitochondria of neural stem/progenitor cells play crucial roles in determining cell fate. Since mitochondrial dysfunction by amyloid pathology is the typical symptom of AD pathogenesis, we aim to study whether mitochondrial dysfunction of neural stem/progenitor cells by amyloid pathology causes the impairment of AHN, and elucidate the molecular mechanism of the phenomenon.

Methods To investigate the effect of mitochondrial dysfunction of neural stem/progenitor cells on neuronal differentiation, we expressed mitochondria-targeted amyloid beta (mitoAβ) in neural stem/progenitor cells *in vitro* and *in vivo*. Proteomic analysis of the hippocampal tissue implicated mitochondrial dysfunction by mitoAβ as a cause of AHN deficits. We identified epigenetic regulators of neural progenitor cells that are regulated by mitoAβ expression or drug-induced mitochondrial toxicity and proposed a link between mitochondria and AHN. **Results** Amyloid pathology characteristically inhibited the neuronal differentiation stage, not the proliferation of neural stem/progenitor cells during AHN in early AD model mice. Mitochondrial dysfunction in neural stem/progenitor cells by expressing mitoAβ inhibited the neuronal differentiation and AHN with cognitive impairment. Mechanistic studies revealed that lysine demethylase 5A (KDM5A) was involved in the neuronal differentiation and could be degraded by mitochondrial dysfunction in neural progenitor cells, thereby inhibiting the differentiation and cognitive functions.

Conclusions These results reveal the new role of KDM5A as a mediator of retrograde signaling, reflecting mitochondrial status, and that the decrease of KDM5A in neural progenitor cells by mitochondrial dysfunction impairs the neuronal differentiation and AHN, finally leading to memory deficits. These findings and its relationship to mitochondrial dysfunction suggest that mitochondrial failure in neural progenitor cells by amyloid pathology closely associates with reduced AHN in AD.

Background

Adult hippocampal neurogenesis (AHN) is the process by which neural stem cells continue to divide and form new neurons even after birth [1]. Adult neurogenesis typically occurs both in the subventricular zone (SVZ) of the lateral ventricle and the subgranular zone (SGZ) of the hippocampus [2]. Neural stem cells (NSC) in the SVZ and the SGZ pass through different stages as they differentiate into mature neurons, which join existing neuronal circuits and contribute to memory and cognitive functions [3]. During AHN, diverse transcription factors and epigenetic regulators cooperatively activate sequential transcription required at each step. Unique marker proteins are known for each cell type, enabling researchers to quantify AHN by investigating the transient expression patterns of marker proteins [4].

The hippocampus is vulnerable to Alzheimer's disease (AD). A recent study showed that AHN continues to occur even in old age but that this process is significantly reduced in the hippocampus of AD patients [5]. Other studies have shown that alteration of AHN is related to pathological features of AD brains and AD model mice, including amyloid pathology in the hippocampus [6-8]. In AD patient brains, the number of immature neurons, doublecortin$^+$ (DCX$^+$) cells, in the SGZ drastically decreased beginning at Braak stage 1 but the number of DCX$^+$ that expressed calretinin, which is transiently expressed in immature neurons at the early differentiation phase, did not change significantly according to Braak stage, indicating that AD pathology has different effects on each stage of AHN and dysregulates neuronal differentiation rather than neural stem/progenitor cells [5]. However, relatively little work has focused on studying the molecular mechanisms underlying the dysregulation of AHN by AD pathology.

Stem cells highly depend on glycolytic metabolism rather than the oxidative phosphorylation that occurs in mitochondria (OXPHOS) [9]. Emerging evidence indicates that beyond energy production, mitochondria centrally coordinate NSC fate decisions during AHN, by managing metabolites, redox signaling, and the epigenetic state of the NSC [10]. Abnormal mitochondrial activity damages the maintenance of stem cells and impairs the fate decisions of stem cells [11, 12]. Disturbance of mitochondrial metabolism in NSC perturbs a progression of AHN, indicating that there is a close relationship between NSC metabolism and differentiation [13].

Mitochondrial retrograde signaling is a pathway that modulates the transcription to maintain cellular homeostasis through retrograde signals originating from mitochondria [14]. Several mediators, such as mitochondrial-derived peptides (MDPs), mitochondrial DNA, and metabolites, can transmit the mitochondrial signals to the nucleus in response to metabolic stress, which in turn regulates transcription [15, 16]. However, the retrograde signaling in which epigenetic regulators required for neuronal differentiation can be regulated by mitochondria has not been elucidated. The stability and turnover of epigenetic regulators could affect transcriptional activity for the fate decisions of stem cells, which deteriorates during senescence and aging [17]. Histone modifying enzymes are controlled by the ubiquitin-proteasome system in response to various stimuli, and this regulation is critical for regulating chromatin structure and gene expression [18]. Here, we show that mitochondrial dysfunction of neural progenitor cells induced by Aβ inhibits neuronal differentiation. Also, we find that mitochondrial damage affects the proteostasis of the epigenetic regulator, lysine demethylase 5A (KDM5A), resulting in the dysregulation of AHN and cognitive decline. Given that mitochondrial dysfunction is characteristic features of the AD brain, mitochondrial damage caused by Aβ is sufficient to induce AHN deficits in AD. Collectively, our results emphasize that mito-nuclear communication through KDM5A in neural progenitor cells functions as a regulatory hub of AHN, and the restoration of mitochondria in neural progenitor cells should be considered as a potential therapeutic target in efforts to ameliorate AHN defects in AD.

Methods

Animals

We used 5XFAD mice (Tg6799; Jackson Laboratory, Stock #006554) that express both mutant human amyloid precursor protein (APP) with the Swedish mutation (K670N, M671L), the Florida mutation (I716V), and the London mutation (V717I) and mutant human presenilin1 (PS1) with M146L and L286V mutations under transcriptional control of mouse Thy-1 promoter. All experiments were performed using female 5XFAD mice. 8-week-old C57BL6 male mice were used for virus injection. All animal experiments and management procedures were performed as outlined in the guidelines of the Institutional Animal Care and Use Committee of Seoul National University.

Real time q-PCR

Total RNA was prepared by using a RNeasy Plus Mini kit (QIAZEN). cDNA was synthesized from 100-200 ng/μl of total RNA by using a Maxime RT PreMix kit (iNtRON Biotechnology, Korea). The real time q-PCR was carried out using KAPA SYBR FAST ABI Prism qPCR kit (KAPA Systems). mRNA levels of interested genes were normalized with 18S ribosomal RNA *(18S rRNA)* levels as a housekeeping gene. PCR primers used in the study were listed in Additional file 1: Table S1.

Real-time oxygen consumption rate measurement

Oxygen consumption rate (OCR) was measured using a Seahorse XF24 analyzer (Seahorse Bioscience). 4×10^4 cells were placed on XF24 cell culture microplates and cultured. The cartridge plate was reacted with XF Calibrant buffer for one day (37 °C, CO_2 free); Analytical medium (1 mM pyruvate, 4 mM glutamine and 25 mM glucose added to the XF basal medium) was prepared immediately before the analysis.

Immunohistochemistry (IHC)

After anesthetizing the mice with cold PBS, brains were extracted and reacted at 4 °C for 24 hrs in 4 % PFA solution. Then, it was reacted at 4 °C for 72 hrs in a 30 % sucrose solution. Brain tissue was cut to 30 μm thickness using Cryostat (Leica) and used in the experiment. Brain sections with hippocampal sections were washed with PBS and then reacted with a solution containing BSA, 0.3 % Triton X-100 and 5% Horse serum to reduce nonspecific responses and enhance antibody permeability. Subsequently, the primary antibody for the target protein was reacted at 4 °C for one day. The proportion of primary antibodies used is as follows; Iba-1 (1:1,000, Wako), 4G8 (1:500). After the reaction with the primary antibody, the IgG secondary antibody (1:500, Invitrogen) conjugated with Alexa-488, 594 or 647 was used at room temperature for 1 hr. DAPI (0.4 μg/ml) was stained for 10 min for the purpose of staining confirmation. Stained brain sections were taken using an LSM 700 confocal laser scanning microscope (Carl Zeiss) and images were analyzed via ImageJ software.

Behavioral analysis experiments

1) Y-maze test

Mice in the control and experimental groups were subjected to spatial adaptation and habituation in a Y-shaped maze one day before the test. In the next day, the Y labyrinth was freely explored for 8 min under the same experimental conditions. The results of the test were analyzed by measuring the percentage of the total number of entrances into the maze, alternating with three different types of mazes (entry without overlapping like ABC).

2) Novel object recognition (NOR) test

Mice injected with LV-scramble siRNA or LV-*Kdm5a* siRNA were habituated to an empty rectangular box for 10 min on day 1. On day 2, two identical objects were placed at the corner of the box, 5 cm away from the same wall, and then individual mice were allowed to explore freely in the box for 10 min. After 4 hrs, one familiar object was replaced with a novel object, and we then measured the time exploring each object, respectively for 8 min. Recognition memory was assessed by the discrimination index, which was analyzed by the percentage of the total time to the exploration time for a novel object during the test session.

3) Passive avoidance task (PAT)

Mice injected with LV-GFP or LV-mitoAβ were allowed to explore in the chamber which is divided into a lighted and dark compartment with a gate. In the acquisition trial, each mouse experienced an electronic shock (0.7 mA, 3 s) only in the dark compartment. On the following day, mice were placed back and explored in the chamber for 300 s. Learning and memory were evaluated by the measurement of the latency time to cross between the compartments.

Transmission Electron Microscope (TEM) Shooting

Hippocampal tissue and HT22 cells expressing mitoAβ were fixed for one day in a mixture of cold 2.5 % glutaraldehyde diluted in 0.1 M phosphate buffer (pH 7.2) and 2 % paraformaldehyde diluted in 0.1 M phosphate or cacodylate buffer (pH 7.2). After the reaction, the tissue and cells were immersed using only epoxy resin, and the samples were loaded into capsules and polymerized for 12 hrs at 38 °C and 48 hrs at 60 °C. Ultramicrotome (RMC MT-XL; RMC Products) was used to cut into thin sections and collected in a copper mold. Thin sections were cut at 65 nm, stained with 4 % uranyl acetate and 4 % lead citrate, and photographed by transmission electron microscopy (JEM-1400; Japan) at 80 Kv.

Mitochondrial ROS Measurement

Mitochondrial-derived reactive oxygen species (ROS) were visualized using MitoSOX Red Mitochondrial Superoxide Indicator (M36008, Invitrogen). The dye is mixed in the cell culture medium at a final concentration of 5 μM. The reaction was carried out at 37 °C for 10 min and then washed with PBS. Fluorescence signals were imaged using fluorescence microscopy (EVOS FL Auto2, Invitrogen).

Mitochondrial membrane potential measurement

The cell culture medium is removed, and TMRM (Invitrogen) is mixed and treated with the cells so that the final concentration is 100 nM in the cell culture medium. After reacting for 30 min at 37 ℃ was photographed using a fluorescence microscope (Olympus).

α-ketoglutarate assay

The amount of α-ketoglutarate was measured using the α-ketoglutarate assay kit (Abcam, ab83431) following the manufacturer's instructions. ReN CX cells expressing GFP or mitoAβ were homogenized with 500 μl Alpha KG assay buffer by pipetting. Cell lysates were centrifuged at 13,000 x g for 5 min, and the resulting supernatant was used for further procedures. To remove proteins, perchloric acid (PCA) solution was added to the homogenate solution (final concentration, 1 M), and the solution was centrifuged at 13,000 x g for 2 min. 2 M KOH solution (34 % of sample volume) was added to precipitate remained PCA, and neutralized sample was centrifuged at 13,000 x g for 15 min. 50 μl of α-ketoglutarate standard or cell lysates were mixed with the reaction mixture including probe and converting enzyme. After incubation at 37 ℃ for 30 min, the results were measured on a PowerWave XS microplate reader (BioTek) at OD570 nm.

Mitochondria fractionation

In order to separate the cytoplasm and mitochondria, the cells were placed in a solution containing 20 mM HEPES, pH 7.5, 250 mM sucrose, 20 mM KCl, 1.5 mM MgCl2, 1 mM EDTA, 1 mM dithiothreitol, and 1 mM phenylmethylsulfonyl fluoride, using a dounce homogenizer. Cell lysates were centrifuged at 600 x g for 10 min to remove undissolved cell debris and nuclei. The supernatant was again centrifuged at 7,000 x g for 10 min at 4 °C, and the resulting pellet was collected as a mitochondria concentrated fraction.

Immunocytochemistry

Cells washed with PBS are fixed in PFA solution for 15 min in 4 % PFA solution. After washing sufficiently with PBS, the antibody was reacted with a solution containing 0.3 % Triton X-100 for 1 hr to improve the accessibility of the antibody. The primary antibody, KDM5A or GFP antibody was added and reacted at 4 °C for one day. After washing with PBS the next day, the cells were reacted with a fluorescent-linked secondary antibody (1:500, Invitrogen) at room temperature for 1 hr. DAPI was stained for 10 min for the purpose of staining confirmation. Labeled cells were transferred to glass slides and photographed with confocal microscopy (LSM700, ZEISS).

Construction of pLentiSyn1.41g-mitoAβ

To prepare the pLentiSyn1.41g-mitoAβ construct, a 222-bp of mitoAβ gene was amplified from pcDNA-mitoAβ by PCR using the following primers: mitoAβ-*EcoR* V-F, 5'-CGGATATCATGTCCGTCCTGACGCCGCT-3' and mitoAβ-*EcoR* V-R, 5'-GCGATATC CTACGCTATGACAACACCGC-3'. The resulting PCR fragment was digested with *EcoR* V and ligated into a lentiviral vector pLentiSyn1.41g under the control of the murine cytomegalovirus immediate early gene promoter. The pLentiSyn1.41g encodes GFP which is expressed by human synapsin 1 promoter.

roduction of pLentiSyn1.41g-mitoAβ

Control and mitoAβ lentivirus were produced as previously described[1]. Human embryonic kidney (HEK) 293T cells were cultured in Dulbecco's modified Eagle's medium (Hyclone Laboratories Inc., Logan, UT, USA) with 10 % fetal bovine serum (Gibco-BRL, Invitrogen, Grand Island, NY, USA) and maintained in a 5 % CO_2 incubator at 37 °C. The lentivirus particles were produced by co-transfection of HEK 293T cells with the following three plasmids using Lipofectamine Plus (Invitrogen): VSV-G, *gag-pol*, and pLentiSyn1.41g-mitoAβ. At 48 hrs post-transfection, culture supernatants containing virus particles were collected and clarified with a 0.45 μm membrane filter (Nalgene, USA) and stored in a -70 °C deep-freezer immediately. Titers were determined with p24 enzyme-linked immunosorbent assays (Perkin-Elmer Life Science) or western blot analyses using a monoclonal anti-p24 antibody (obtained from the AIDS Research and Reference Reagent Program, National Institutes of Health, Bethesda, MD, USA). In our routine preparation, the titers were ≒ 10^7 transduction units (TU) per mL without further concentration. For stereotaxic injection, the lentivirus particles were concentrated by ultracentrifugation on a 20 % sucrose cushion (2 hrs at 50,000 × *g*) at 4 °C.

Stereotaxic injection

8-week-old C57BL/6 male mice were anesthetized with zolazepam and tiletamine (30mg/kg; Virbac), mixed with xylazine (10mg/ml; Bayer Korea), and then fixed in a stereotaxic instrument (Neurostar, Germany). Coordinate for the injection was set at the AP axis -2.0 mm, the ML axis 1.3 mm and the DV axis 2.1 mm from bregma of the skull. A total volume of 2 μl (1×10^7 titer of lentivirus) was injected into the dorsal DG of the hippocampus, using an automatic microinjector, at a rate of 0.2 μl/min. After reaching the desired coordinates, a Hamilton syringe was left in place for 10 min to prevent the backflow of the virus liquid.

Hippocampal neural stem cell culture

Hippocampal neural stem (HCN) cells derived from adult rat were cultured at 37°C and 5% CO_2 on dishes coated with 10 mg/mL poly-L-ornithine (Sigma-Aldrich, P3655) and 5 mg/mL mouse laminin (Corning, 354232), and maintained on Dulbecco's modified Eagle's medium (DMEM)/F-12 (Invitrogen, 12400-024) containing 5 mg/L insulin (Sigma-Aldrich, I6634), 100 mg/L apo-transferrin (Prospec, PRO-325), penicillin (100 U/L)/streptomycin (100 mg/L) (Hyclone, SV30010), 16 mg/L putrescin (Sigma-Aldrich, P5780), 30 nM sodium selenite (Sigma-Aldrich, S1382), 20 nM progesterone (Sigma-Aldrich, P0130), and 20 ng/ml basic fibroblast growth factor (bFGF) (Peprotech, #100-18B) [19]. For differentiation, HCN cells were plated onto coated dishes at a density of ~ $0.5\times10^5/cm^2$, and 24 hrs later, culture medium was changed with media containing 1 μM retinoic acid (Enzo, BML-GR100), 5 μM forskolin (Enzo, BML-CN100), and 0.1% fetal bovine serum (Tissue Culture Biologicals, 101) [20]. The medium was changed half every 2 days until experiment.

Chromatin immunoprecipitation (ChIP)

ReN CX cells or differentiated cells (after 5 days) were fixed with 1 % formaldehyde at room temperature for 10 min. After cross-linking reactions, the fixation was stopped by adding 1 M glycine solution to be at a final concentration of 125 mM. The solution was centrifuged at 3,000 rpm for 5 min, and the resulting pellet was then washed 3 times with ice-cold phosphate-buffered saline (PBS). Cell pellets were suspended with lysis buffer (sc-45000, Santa Cruz) and centrifuged at 3,000 rpm for 5 min. Crude nuclear extract was re-suspended with high salt lysis buffer (sc-45001, Santa Cruz) and sonicated 15 times by 30 s burst, each followed by 1 min incubation on ice. The sample was centrifuged at 14,000 rpm for 10 min, and then the supernatants containing chromatin were diluted 1:10 with the dilution buffer containing 0.01 % SDS, 1.1 % Tritonx-100, 1.2 mM EDTA, 16.7 mM Tris pH 8.1, 167 mM NaCl, and proteinase inhibitor cocktail. For preclearing the chromatin samples, 50 µl Protein A/G PLUS-Agarose beads (sc-2003, Santa Cruz) were added to the samples and incubated at 4 ℃ for 30 min. To precipitate agarose beads, the chromatin solution was centrifuged at 12,000 rpm for 20 s. 5 – 10 µg antibodies were added in the precleared chromatin solution and incubated overnight at 4 ℃. On the following day, 50 µl Protein A/G PLUS-Agarose beads were added and incubated at 4 ℃ for 2 hrs. To collect the beads, the solution was centrifuged at 12,000 rpm for 20 s. After the beads were washed with high salt lysis buffer and wash buffer (sc-45002, Santa Cruz), the beads were suspended with 500 µl of elution buffer with 20 µl of 5 M NaCl. Cross-linking was reversed by heating at 65 ℃ for 4 hrs. To isolate DNA fragments, the supernatants were mixed with 500 µl phenol/choloroform solution

Library preparation and sequencing

The construction of library was performed using NEBNext® Ultra™ DNA Library Prep Kit for Illumina (New England Biolabs, UK) according to the manufacturer's instructions. Briefly, the chipped DNA was ligated with adaptors. After purification, PCR reaction was done with adaptor-ligated DNA and index primer for multiplexing sequencing. Library was purified by using magnetic beads to remove all reaction components. The size of library was assessed by Agilent 2100 bioanalyzer (Agilent Technologies, Amstelveen, The Netherlands). High-throughput sequencing was performed as paired-end sequencing (101 bp) using HiSeq 2500 (Illumina, Inc., USA).

ChIP sequencing data analysis

The reads were trimmed and aligned using Bowtie2 (Langmead and Salzberg, 2012). Bowtie2 indices were generated from genome assembly sequence or the representative transcript sequences during the alignment of the reads to the genome or transcriptome, respectively. With the mapped reads, we used MACS2 (Model-base Analysis of ChIP-seq) for identifying the peaks representing DNA binding of KDM5A. Transcription factor binding sites enriched in the peaks were identified using HOMER (Hypergeometric Optimization of Motif EnRichment), a software suite for ChIp-Seq analysis. Gene classification was performed based on the results from functional enrichment analysis using g:Profiler (https://biit.cs.ut.ee/gprofiler/).

Protein extraction

Collected hippocampal tissues from two control (LV-GFP) and two Aβ (LV-Mito-Aβ) groups were individually pulverized using Covaris CP02 Cryoprep device (Covaris, Woburn, MA). Briefly, each tissue piece was placed in a Covaris tissue bag (Covaris, 430487), and the bag was placed in a liquid nitrogen for 30 s. The frozen tissue was subsequently pulverized at impact level 2. We then added 500 µl of lysis buffer (4%SDS in Tris-HCl pH 7.6 and phosphatase inhibitor) to the tissue powder, which were subsequently sonicated using a probe sonicator (Q55, QSONICA, Newtown, CT) at 30 W on ice for 30 s. The tissue lysate was centrifuged at 16,000 x g for 10 min, and supernatants was transferred to a siliconized low-retention tube. Protein concentration was then measured using the BCA protein assay (Pierce, Rockford, IL).

Protein digestion

All hippocampal proteins were digested by the filter aided sample preparation (FASP) method [21] with a slight modification. Briefly, hippocampal proteins were reduced with SDT buffer (4 % SDS in 0.1 M Tris-HCl pH 7.6 and 0.1 M DTT) at 37 °C for 45 min by shaking at 300 rpm followed by boiling for 10 min at 95 °C on a thermomixer (Eppendorf, Hamburg, Germany). The protein sample was centrifuged at 16,000 x g for 5 min and transferred to a YM-30 microcon filter, in which the protein sample was mixed with 200 µl of UA buffer (8 M urea in 0.1 M Tris-HCl pH 8.5). The protein samples were then centrifuged at 14,000 x g at 20 °C for 60 min to remove SDS. This step was repeated three times. After alkylation for 25 min with 100 µL of 0.05 M iodoacetamide in 8 M urea at room temperature in the dark, the filter was centrifuged at 14,000 x g for 30 min, followed by washing with 200 µl of UA buffer four times. 100 µL of 0.05 M ammonium bicarbonate was added to the filter before it was centrifuged at 14,000 x g for 30 min for buffer exchange. This step of buffer exchange was repeated twice. Subsequently, sequencing grade modified trypsin (Promega; Madison; WI) was added to protein samples on the filter at an enzyme to protein ratio of 1: 50 (w/w), and the proteins were digested overnight at 37 °C. After the first digestion, the second digestion was carried out with trypsin (1: 100 w/w) at 37 °C for 6 hrs. The concentration of hippocampal peptide samples was measured by the BCA assay.

Isobaric Tag for Relative and Absolute Quantitation (iTRAQ) labeling and fractionation

The hippocampal peptide samples from two LV-GFP and two LV-mitoAβ injected groups (700 µg each) were labeled with 4-plex iTRAQ reagent (AB Sciex, Foster City, CA) according to the manufacturer's instructions. The two LV-GFP groups were labeled with 114/116 iTRAQ reagents, respectively, while two LV-mitoAβ groups were labeled with 115/117 iTRAQ reagents, respectively. All labeled peptide samples were then pooled and dried by vacuum centrifugation. The pooled iTRAQ labeled peptide sample was fractionated using Agilent 1269 Infinity HPLC system (Agilent, Palo Alto, CA) as previously described [22]. The Xbridge C18 column (4.6 mm × 250 mm, 130 Å, 5 µm, Waters, Milford, MA) and a guard column (4.6 mm × 20 mm, 130 Å, 5 µm) were used for the peptide separation. The peptide fractionation was performed with a 115 min gradient at a flow rate of 500 µL/min: at 0 % solvent B [10 mM TEAB in 90 % ACN (pH 7.5)] for 10 min, from 0 % - 5 % solvent B in 10 min, from 5 % to 35 % in 60 min, from 35 % - 70 % in 15 min, at 70 % solvent B for 10 min, from 70 % - 0 % solvent B in 10 min, and at 0 % solvent over 15

min. A total of 96 fractions were collected in every 1 min from 15 min to 110 min, and they were non-contiguously concatenated into 24 fractions (i.e., #1-#25-#49-#73, #2-#26-#50-#74, …, #24-#48-#72-#96). The resultant 24 fractions were dried by vacuum centrifugation. 10 µg of each fraction was used for global proteome profiling, and the remaining samples were used for phosphopeptide enrichment by immobilized-metal affinity chromatography (IMAC) [22]. For IMAC experiment, the 24 fractions were further concatenated into 12 fractions by pooling two adjacent fractions (i.e., #1-#2, #3-#4, …, #23-#24) before drying and storing at -80 °C.

Phosphopeptide enrichment

For phosphopeptide enrichment, 1.5 mL of Ni-NTA bead slurry (36113, Qiagen, Valencia, CA) was washed three times with 1.2 mL of deionized water (DIW), and Ni^{2+} ions were removed from NTA bead by adding 1.2 mL of 100 mM EDTA (pH 8.0) and mixing for 30 min on an end-over-end rotator (SB3, Stuart). After removal of the EDTA solution, NTA beads were washed three times with 1.2 mL of DIW and then reacted with 1.2 mL of 10 mM aqueous $FeCl_3$ solution for 30 min on an end-over-end rotation. The Fe^{3+}-NTA beads were washed with 1.2 mL of DIW three times and resuspended in 1.2 mL of 1:1:1 ACN/MeOH/0.01 % acetic acid for aliquoting into 12 microcentrifuge tubes and each of the Fe^{3+}-NTA beads was washed with 400 µL of binding buffer (80 % ACN/0.1% TFA). Each of the 12 fraction samples was then resuspended in 500 µL of binding buffer and individually transferred to a tube of the aliquoted Fe^{3+}-NTA beads. The binding reactions of the 12 aliquoted peptide samples were performed in parallel for 30 min on an end-over-end rotation. After the binding reaction, the beads were washed with 500 µL of binding buffer for four times. The bound phosphopeptides were eluted by incubating in 125 µL of 1:1 ACN/2.5 % ammonia in 2 mM phosphate buffer (pH 10) for 1.5 min. The eluted phosphopeptides were acidified with 10 % TFA to pH 3.5 - 4.0 immediately before drying.

LC-MS/MS experiments

The 24 fraction global peptide and 12 fraction phosphopeptide samples from hippocampal tissues were individually analyzed using a proteome profiling platform (at the Center for Proteogenomic Research, kore) that consists of a dual-online UPLC system (Waters, Milford, MA) [23] online coupled with Q-Exactive orbitrap mass spectrometer (ThermoScientific, Bremen, Germany). The dual-online UPLC system was equipped with two analytical columns (75 µm i.d. x 360 µm o.d, 100 cm) and two solid phase extraction (SPE) columns (150 µm i.d. x 360 µm o.d, 3 cm), and all columns were manufactured by slurry packing of C18 materials (3 µm diameter, 300 Å pore size, Jupiter, Phenomenex, Torrance, CA, USA) as previously reported [24]. The column was heated to 60 °C, and a flow rate was set to 300 nL/min [24]. The global peptides were separated by a 180 min linear gradient (1-40 % solvent B over 160 min, 40 - 80 % over 5 min, 80 % for 10 min and holding at 1 % for 5 min), and phosphopeptides were separated by a 240 min gradient (1 % to 50 % solvent B over 220 min, 50 % - 80 % solvent B over 5 min, 80 % solvent B for 10 min and holding at 1 % for 5 min). The solvent A and B were 0.1 % formic acid in water and 0.1 % formic acid in acetonitrile, respectively. The eluted peptides from LC were ionized at 2.4kV, and the desolvation capillary temperature was kept at 250 °C. Full MS data was acquired between 400 and 2,000 m/z at the

resolution of 70,000, and the automated gain control (AGC) target value was set to 1.0 x 10^6 with a maximum ion injection time of 20 ms. The tandem mass (MS/MS) data were obtained using a data-dependent acquisition (DDA) mode, and isolation of the most abundant top 10 ions was performed within ± 0.8 Th window. The isolated precursor ion was fragmented at a normalized collision energy (NCE) of 30 for higher energy collisional dissociation (HCD). The resolution of MS/MS data was set to 17,500, and AGC target value was to 1.0 x 10^6 with a maximum ion injection time of 60 ms.

LC-MS/MS data analysis

The LC-MS/MS data from global proteome and phosphoproteome profiling experiments were processed with the PE-MMR (Post-experiment monoisotopic mass refinement) method as previously described [25]. The resultant tandem mass data were searched against a mouse uniprot database (April, 2014; 51,388 entries) through MS-GF+ (v9387) search engine [26] with the search parameters: Semi tryptic, 10 ppm precursor mass tolerance, iTRAQ (+144.102063 Da) modification of lysine and N-termini and carbamidomethylation (+57.0214 Da) of cysteine as static modifications; and methionine oxidation (+15.994915 Da) as a variable modification. For phosphopeptide search, phosphorylation (+79.966) to serine/threonine/tyrosine was set as an additional variable modification. The identified phosphopeptides were further subjected to the unique mass class (UMC) filtering to localize the sites of phosphorylation as previously described [27] . The search results from the 24 MS/MS data sets of global proteome and the 12 MS/MS data sets from phosphoproteome were combined, respectively. Peptides were finally identified from the peptide spectrum matches (PSMs) with the false discovery rate (FDR) less than 0.01 and used for the downstream analyses. The identified non-redundant peptides were used to obtain protein groups by a bipartite graph analysis [28]. Among the component proteins of each protein group, the protein of the highest number of associated peptides was selected as the representative of the protein group. When multiple proteins had the same number of non-redundant peptides, the protein of a higher protein sequence coverage was chosen as the representative protein. Additionally, a protein having any unique peptides was selected as a separate representative protein. For global proteome analysis, two or more sibling non-redundant peptides were required for protein group identification. In the case of the phosphoproteome analysis, all protein groups identified by the phosphorylated peptides were used.

Identification of differentially expressed peptides and proteins

The intensities of the iTRAQ reporter ions for hippocampus samples from two LV-GFP and two LV-Mito-Aβ injected mice were normalized using the quantile normalization method [29]. Using the normalized intensities of each peptide, we performed Student t-test and calculated $\log_2$-median-ratios (fold-changes) for LV-Mito-Aβ to LV-GFP groups. We next estimated the null hypothesis distributions of these values by performing random permutations of the samples and computing t-statistic values and $\log_2$-median-ratios as previously described [30]. An adjusted p value was calculated for a t-statistic value for each peptide by two sample test using the empirical distribution. Differentially expressed (DEpeptides) and phosphorylated peptides (DPpeptides) were then identified as the peptides with $p < 0.05$ from the two sample t-test and $\log_2$-median-ratios > 95^{th} percentiles in its empirical null distribution (1.32- and 1.58-

fold for global and phosphoproteome profiles, respectively). The DEPs were identified as the proteins with at least two unique DEpeptides showing consistent up- or down-regulation in LV-Mito-Aβ injected mice. DPpeptides with more than two spectral counts were used for the subsequent analyses, and differentially phosphorylated proteins (DPPs) were defined as the proteins containing the DPpeptides.

GOBP association analysis.

We built a network model describing the links among the 586 GOBPs enriched by the three sets of proteins affected by LV-mitoAβ: 1) 281 up- and 2) 218 down-regulated proteins and 3) 191 DPPs. For each pair of the 586 GOBPs (GOBP1 with n proteins, GOBP2 with m proteins, and k shared proteins between GOBP1 and 2), we computed the similarity score as $2k/(n+m)$ and connected the two GOBPs with the similarity score > 0.52 (99 % of the null distribution for the similarity score). This procedure resulted in 43 connected subnetworks, called functional modules. The importance (weighted degree) of GOBPs in each module was estimated by summing the similarity scores of its interactors in the corresponding subnetwork. The GOBPs were then ranked by their weighted degrees such that the top-ranked GOBP has the largest weighted degree (i.e., a hub-like term). Also, the key GOBPs should be highly enriched with up- and down-regulated proteins and DPPs. Thus, we evaluated the enrichment of the GOBPs in each module using EASE scores obtained from DAVID [31]. The GOBPs in each module was then ranked such that the top-ranked GOBP has the largest enrichment score. After summing the two ranks from the weighted degrees and the enrichment scores, finally, the key GOBP in each module was selected as the top-ranked one based on the summed ranks.

Statistical analysis

All values are expressed as mean ± standard error of the mean (SEM) from. The significant differences between two groups were analyzed by Student's unpaired t test. In three or more groups the significant differences were evaluated by one-way ANOVA or two-way ANOVA test. Statistical significance is displayed as: N.S., not significant; * $P < 0.05$; ** $P < 0.01$; *** $P < 0.001$; **** $P < 0.0001$.

Results

5XFAD mice exhibit inhibited neuronal differentiation and AHN deficits

To investigate the alteration of AHN in the hippocampus of 5XFAD mice, we examined the expression of cell markers at the distinct stages of AHN in the SGZ. Neural progenitors and neuroblasts express PCNA at the early and middle stages of AHN; after exiting a proliferation stage, immature neuroblasts differentiate into fully mature neurons expressing DCX in the later stage of AHN [32]. The expression of DCX was found to be significantly reduced in the hippocampus of 6-week-old 5XFAD mice compared to in that of wild-type mice, but there was no significant difference in the number of $PCNA^+$ cells in the SGZ (Figures 1A-1C). Consistent with the PCNA results, the $SOX2^+$ cell number in the SGZ (a marker for proliferating neural stem and progenitor cells) did not differ between 5XFAD and wild-type mice (Figures 1D and 1E).

To further assess the maturity stages of AHN, we analyzed the morphological features of axons projecting from mature granule cells. We labeled axon fibers with an antibody against synaptoporin, which is exclusively enriched in granule cells of the hippocampus; these cells were specifically labeled along with mossy fibers running in both directions toward the CA3 cell layer (superficial mossy fiber, SMF; and infrapyramidal mossy fiber, IMF) [33]. The synaptoporin intensity, IMF length, and IMF/SMF ratio were decreased in 6-week-old 5XFAD mice compared to in wild-type mice, indicating that the maturation of granule cells declined in early AD (Figures 1F and 1G). Although extracellular amyloid plaques are observed in the 5XFAD mouse hippocampus beginning at approximately 16 weeks of age [34], we detected a non-aggregated form of Aβ and intra-neuronal accumulation of Aβ in granule cells of the SGZ in 6-week-old 5XFAD mice, as assessed by Western blot analysis and immunohistochemistry (Figures 1H and 1I). In rodents, AHN continues actively until about 24 weeks of age; thereafter, the hippocampal niche for AHN typically decreases with age. In humans, continuous AHN occurs throughout life, resulting in the replacement of most retained granule cells [35, 36]. AHN was decreased still in 20-week-old 5XFAD mice compared to in wild-type (Additional file 2: Figure S1). Taken together, these results indicate that Aβ, not amyloid plaques, could impede AHN by inhibiting the neuronal differentiation process rather than by affecting neural stem or progenitor cells.

MitoAβ impairs the structure and function of mitochondria

We previously reported that mitochondria-targeted Aβ (mitoAβ), induced as found in the AD brain, could induce mitochondrial dysfunction, resulting in apoptotic cell death [37]. In addition to cell death, the accumulation of Aβ in the mitochondria may contribute to reduced AHN in AD. To verify that mitochondria contribute to stem cell fate decisions and to determine the effect of mitochondrial dysfunction on AHN in AD, we induced to express mitoAβ to characteristically disrupt only the mitochondria. MitoAβ consists of Aβ, a signal peptide for translocation into mitochondria, and eGFP as a marker for vector expression (Figure 2A). The expression of mitoAβ could be induced by both transfection and viral transduction (Figures 2B and 2C). In addition, the presence of mitoAβ in mitochondria, not in the cytosol, was confirmed through the mitochondria-enriched fractionation (Figure 2C). Before investigating the structural and functional defects of mitochondria caused by mitoAβ, HT22 mouse hippocampal neuronal cells expressing GFP or GFP/mitoAβ via lentiviral transduction (LV-GFP and LV-mitoAβ) were separated by fluorescence-activated cell sorting (FACS) to generate a homologous infected cell population (Figure 2D). Transmission electron microscopy imaging revealed the altered cristae structure in mitoAβ-expressing cells (Figure 2E). We also examined functional abnormalities of the mitochondria by measuring cellular respiration rate with a Seahorse XF analyzer (Figure 2F). Our results confirmed that mitoAβ lowered the maximum respiration rate and level of ATP production, but exerted no significant effects on the mitochondria-independent respiration rate (Figures 2G-2I). These results indicate that Aβ accumulated specifically inside the mitochondrial matrix causes structural and functional abnormalities of the mitochondria.

MitoAβ inhibits neuronal differentiation

To investigate whether mitoAβ-induced mitochondrial damage of neural stem cells inhibits their differentiation into neurons, we expressed mitoAβ in adult neural stem cells isolated from the adult hippocampus. GFP^+ neural stem cells, as a control group, differentiated well into neurons with normal forms of neurites; in contrast, GFP/$mitoAβ^+$ cells had short and immature neurites, indicating uncompleted differentiation status (Figures 3A and 3B). Likely as a result of this incomplete differentiation, GFP/$mitoAβ^+$ cells exhibited lower cell viability than the control group (Figure 3C). These data showed that the expression of mitoAβ could inhibit the neuronal differentiation process, suggesting that mitochondrial function is an essential regulator for the differentiation of neural stem cells.

To further examine the effect of mitochondrial damage on AHN *in vivo*, we infused LV-GFP or LV-mitoAβ into the SGZ of the hippocampi of 8-week-old C576BL/6 mice. Two months after lentiviral transduction, the AHN status was analyzed and behavioral tests were performed. In the control group, GFP^+ cells extended long apical dendrites and migrated toward the upper granule cell layer. In contrast, GFP/$mitoAβ^+$ cells were confined to the SGZ and exhibited highly branched neurites similar to those of the radial glial-like stem cells observed in the early stage of AHN (Figure 3D and 3E).

To investigate whether decreased AHN by mitoAβ reduces differentiation into mature neurons in the hippocampus, we examined the expression of several synaptic proteins, including the granule cell-specific protein, synaptoporin. There was no change in the expression of synaptotagmin and PSD95, but synaptoporin was significantly reduced in the LV-mitoAβ group (Figure 3F). To further trace the fate of GFP/$mitoAβ^+$ cells, cell-type-specific marker proteins and GFP were labeled together. In the control group, most cells were negative for glial fibrillary acidic protein (GFAP), the marker for neural stem cells in the SGZ, and SOX2. In contrast, GFP/$mitoAβ^+$ cells were positive for both GFAP and SOX2, but not for the mature differentiated neuron-specific protein, calbindin (Figure 3G and 3H). These results indicate that mitoAβ-expressing cells failed to properly differentiate into neurons at the neural stem/progenitor stage.

Although stereotactic surgery could activate glial cells in the ipsilateral hemisphere compared to in the contralateral hemisphere, as confirmed by staining for GFAP or Iba-1 (representing astrocytes or microglia, respectively), mitoAβ led to no significant effect on glial activation (Additional file 2: Figures S2A-S2D). When mitoAβ was expressed in the hippocampus, Western blot analysis revealed no significant alterations of the mitochondrial constituent proteins, Atp5a, Hsp60, and Tomm20 (Additional file 2: Figure S2E). Similarly, staining of Tomm20 protein, which was found in both GFP^+ and GFP/$mitoAβ^+$ cells, showed no reduction by mitoAβ (Additional file 2: Figure S2F). Although there was no quantitative change in the tested mitochondrial proteins, the mitochondrial structural breakdown observed *in vitro* was also examined at the tissue level. We observed mitochondria with the disrupted cristae structure in the hippocampus where mitoAβ was expressed (Additional file 2: Figure S2G).

Inhibition of AHN by mitoAβ causes memory impairment

Hippocampus-dependent cognitive functions were tested to investigate whether the inhibition of AHN by mitoAβ was sufficient to cause memory impairment. After 2 months of lentiviral transduction, 4-month-

old mice were subjected to three different behavioral analyses: passive avoidance test (PAT), Y-maze test, and contextual fear conditioning (CFC) test. The Y-maze test to evaluate the effect of mitoAβ on spatial memory revealed that LV-mitoAβ mice exhibited lower spontaneous alternation compared with LV-GFP mice (Figure 3I). In the CFC test, we observed a significant decrease in the freezing time of LV-mitoAβ mice compared with LV-GFP mice (Figure 3J). Finally, the PAT to evaluate memory retention showed that LV-GFP or LV-mitoAβ mice exhibited similar learning abilities during the acquisition phase. However, on the following day, LV-mitoAβ mice showed a shorter latency time in the retention trial compared to LV-GFP mice (Figure 3K). Taken together, all these data suggest that the expression of mitoAβ in adult neural stem cells is sufficient to cause AHN deficits and impair hippocampus-dependent cognitive functions.

Hippocampal proteome alterations triggered by mitoAβ are primarily associated with AHN

To identify cellular pathways altered by mitoAβ, we performed global proteomic and phosphoproteomic profiling of hippocampal tissues from LV-GFP- or LV-mitoAβ-injected mice using liquid chromatography (LC)-tandem mass spectrometry (LC-MS/MS) analysis (Figure 4A). We identified 499 differentially expressed proteins (DEPs; 281 up-regulated and 218 down-regulated, $P < 0.05$) and 236 differentially phosphorylated proteins (DPPs; 111 up-regulated and 125 down-regulated, $P < 0.05$) in LV-mitoAβ hippocampal tissues, compared to in LV-GFP controls (Additional file 3: Table S2).

We next identified 586 Gene Ontology Biological Processes (GOBP) enriched by the three sets of proteins: 1) 281 up-regulated proteins, 2) 218 down-regulated proteins, and 3) 191 DPPs (Additional file 3: Table S2). To investigate the functional modules affected by mitoAβ, we built GOBP association networks based on relationships among the 586 GOBPs as described in Methods. The GOBP networks revealed the following functional modules affected by mitoAβ (Figure 4B): 1) neurogenesis and transport, 2) regulation of cell death, 3) response to nitrogen compound, 4) regulation of neuron projection development, 5) cell junction, 6) cellular homeostasis, 7) learning and memory, 8) nitric oxide metabolic process, and 9) regulation of telomere maintenance. Interestingly, among these nine functional modules, the ‘neurogenesis and transport’ module was found most significantly affected by mitoAβ. Among the GOBPs in this module, we then selected GOBPs that were judged as being consistent with the phenotypes observed in the mitoAβ-expressing hippocampus and adult neural stem cells. Of these selected GOBPs, neurogenesis, axon development, and cytoskeleton organization were commonly enriched by all three sets of proteins, whereas brain development, long-term synaptic potentiation, and cell migration were specifically enriched by the down-regulated proteins (Figure 4C). These results support our finding that mitoAβ strongly dysregulates AHN at the global proteome level.

Mitochondrial damage in neural progenitor cells induces KDM5A degradation

The epigenetic regulation of gene expression can be controlled by the metabolic status of a cell and the resulting metabolites [38]. Jumonji-C domain-containing histone demethylase (JHDM), such as lysine demethylase 5A (KDM5A), utilizes α-KG as a cofactor and promotes the demethylation of histones [39]. AMP-activated protein kinase (AMPK) is responsive to the ATP/AMP ratio and phosphorylates histones, while O-linked N-acetylglucosamine transferase (OGT) is associated with the glucose and hexosamine

biosynthetic pathways, wherein it glycosylates histones [38, 40, 41]. To further elucidate the molecular mechanisms underlying the impairment of neuronal differentiation by mitoAβ, we examined the expression of epigenetic modulators associated with cellular metabolism (KDM5A, AMPK, and OGT) in mitoAβ-expressed ReNcell CX, immortalized human neural progenitor cells. MitoAβ expression decreased the protein levels of KDM5A, but not those of AMPK and OGT (Figures 5A-5C). Interestingly, however, mitoAβ expression led to no decrease in the mRNA levels of KDM5A, indicating that the mitoAβ-induced decrease of KDM5A at the protein level is mediated by proteolysis (Figure 5D).

Next, we examined several phenotypes in mitoAβ-expressing neural progenitor cells. α-KG, which is used as a cofactor of KDM5A, was increased by mitoAβ in neural progenitor cells (Figure 5E). This is consistent with previous reports that the activity of the α-KG dehydrogenase complex is inhibited by Aβ in AD brains, increasing α-KG [42, 43]. MitoAβ expression did not alter mitochondria-derived ROS (Additional file 2: Figure S3A) but did lower the mitochondrial membrane potential (Figure 5F). MitoAβ expression did not alter the levels of characteristic genes of neural progenitor cells (*SOX2*, *MSL1*, *TUJ1*) (Additional file 2: Figure S3B) or the proliferation of neural progenitor cells (Additional file 2: Figure S3C). There was no mitochondrial dysfunction-related change in transcription factors required for the differentiation process (Additional file 2: Figure S3D).

Consistent with the above findings, we also observed decreases of KDM5A when we treated neural progenitor cells with the mitochondrial stress drugs, antimycin A and FCCP. The mitochondrial dysfunction induced by these drugs promoted the proteasome-mediated degradation of KDM5A, and this phenotype was rescued by the proteasome inhibitor, MG132 (Figure 5G). However, the decrease of KDM5A was not rescued by the autophagy flux inhibitor, bafilomycin A (Figure 5G). The ubiquitination of KDM5A was increased by FCCP (Figure 5H). These findings indicate that mitochondrial dysfunction activates the proteasome system and leads to a decrease of KDM5A.

Interestingly, FCCP treatment to mouse hippocampal neurons induced no degradation of Kdm5a (Additional file 2: Figure S4A). Moreover, both FCCP and antimycin A failed to significantly affect the cell viability of neural progenitor cells, but caused cytotoxicity in mouse hippocampal neurons (Additional file 2: Figure S4B). These results suggest that the resistance to mitochondrial damage and the mitochondria-based signaling pathway to regulate the degradation of KDM5A may differ depending on the cell type.

To find out whether the damage of mitochondria of neural progenitor cells affects the differentiation process into neurons, neural progenitor cells were treated with mitochondrial stress drugs for 12 hrs and then were differentiated for 12 days. Neural progenitor cells treated with FCCP or oligomycin A expressed less DCX protein levels after differentiation, supporting the idea that mitochondrial dysfunction of neural progenitor cells dysregulates neuronal differentiation (Figure 5I).

To further explore the roles of KDM5A as an epigenetic regulator, its target genes in neural progenitor and differentiated cells were investigated by chromatin immunoprecipitation sequencing (ChIP-seq) (Additional file 4: Table S3). Notably, according to the enrichment analysis of GOBPs, the target genes of KDM5A were mainly associated with neuronal differentiation-associated processes, such as cellular

component morphogenesis, cellular morphogenesis involved in differentiation, and neuron differentiation (Figure 5J; Additional file 5: Table S4). 43 genes that belong to 7 GOBPs (Figure 5J) in common were transcribed more actively in differentiated cells than in neural progenitor cells (Figure 5K). The mRNA levels of *BDNF* and *MEF2A*, previously known to be important for neurogenesis, were reduced both in mitoAβ-expressing and FCCP-treated differentiated cells (Figure 5L). Taken together, these data suggest that the mitochondrial-dysfunction induced decrease of KDM5A in neural progenitor cells dysregulated the transcription of genes essential for neuronal differentiation, such as *BDNF* and *MEF2A*, thereby inhibiting the differentiation of these cells into neurons.

Degradation of KDM5A is induced by various reactions from mitochondrial damage

The fundamental function of mitochondria is to regulate calcium homeostasis in the cytoplasm [44]. When mitochondrial damage interferes with the buffering of calcium ions, cytosolic calcium levels increase and activate various calcium ion-regulated kinases, including Ca^{2+}/calmodulin-dependent protein kinase II (CaMKII). Neural progenitor cells treated with an inhibitor of ATP synthase, oligomycin A, exhibited activation of CaMKII and the down-regulation of KDM5A. When these cells were both treated with oligomycin A and an inhibitor of CaMKII (KN-93), KDM5A protein levels were restored, indicating that the signaling pathway through which oligomycin A decreases KDM5A depended on calcium and CaMKII (Additional file 2: Figure S5A and S5B). Similar to the effects of mitoAβ expression and FCCP treatment, NPC cells treated with oligomycin A expressed less BDNF and MEF2A during the differentiation (Additional file 2: Figure S5C). However, as there was no change in mitochondrial proteins and transcription factors required for the differentiation by oligomycin A treatment, it was confirmed that KDM5A-specific decrease was caused by mitochondrial damage (Additional file 2: Figure S5D and S5E). FCCP also promoted the down-regulation of KDM5A, but KN-93 did not restore decreased KDM5A protein levels by FCCP (Additional file 2: Figure S5F). These results indicate that mitochondrial dysfunction appears to induce KDM5A degradation through various signaling pathways.

Inhibition or knockdown of KDM5A in neural progenitor cells reduces neuronal differentiation and cognitive function

We next used the KDM5A inhibitor, CPI-455, to specifically examine whether a decrease of KDM5A impairs neuronal differentiation. Neural progenitor cells undergoing differentiation were treated with CPI-455, and various parameters were examined. Our results revealed that DCX levels were reduced after the differentiation under the KDM5A-inhibited condition (Figure 6A). The KDM5A target genes, *BDNF* and *MEF2A*, were also reduced by CPI-455, as well as by mitoAβ and mitochondrial stress drugs (Figure 6B). To verify the effect of *KDM5A* knockdown on neuronal differentiation, we infused *Kdm5a*-siRNA lentiviruses into the DG of 8-week-old C57BL/6 mice and traced the final fate of *Kdm5a*-knockdown cells during AHN. At 4 weeks after viral transduction, most of the *Kdm5a*-knockdown cells failed to co-stain with DCX in the SGZ compared to the scramble-siRNA-transduced group (Figure 6C). We next used three different behavioral tests to examine the effect of *Kdm5a* knockdown on cognitive functions. In the novel object test (NOR), the *Kdm5a*-knockdown group showed a lower discrimination index compared to the

control group (Figure 6D and 6E). There was no significant difference in the total exploration time between the two groups (Figure 6F). In addition, mice in the *Kdm5a*-knockdown group showed significantly impaired spatial memory in the Y-maze test (Figure 6G and 6H). Our results suggest that knockdown of KDM5A impairs neuronal differentiation and is sufficient to cause cognitive impairment.

Discussion

AHN occurs throughout the human lifespan and is reported to be drastically lower in AD patients and AD model mice than in normal groups [5, 45, 46], but relatively little was known about the molecular mechanisms underlying the lack of AHN in AD. In this study, we show that the loss of AHN in AD is associated with amyloid pathology and mitochondrial dysfunction caused by Aβ. In AD patient brains, AD pathology has different effects on the various stages of AHN and dysregulates neuronal differentiation rather than neural stem/progenitor cells [5]. As in AD patients, we found that DCX^+ cells were remarkably reduced in the hippocampi of 6-week-old 5XFAD mice even before the initiation of amyloid plaque deposition, whereas there was no significant difference in $PCNA^+$ and $SOX2^+$ cells, indicating that neuronal differentiation during AHN is vulnerable to soluble Aβ from the early stage of AD.

The mitochondrial regulation of stem cells is crucial for AHN and decisions related to stem cell fate. Given the hippocampal niche where AHN occurs, we hypothesized that, in AD brains, mitochondrial dysfunction of neural stem/progenitors by Aβ dysregulates neuronal differentiation, thereby leading to AHN deficits. Using previously developed mitoAβ [37], which specifically accumulates in mitochondria, we confirmed that the expression of mitoAβ in neural progenitor cells inhibited the formation of neurites during the differentiation into neurons and blocked the normal completion of the neuronal differentiation process *in vitro* and *vivo*. Aβ has toxic effects on the mitochondria of neural stem/progenitor cells, as previously reported. Our results strongly support the idea that mitochondria of neural progenitor cells are central regulators of differentiation.

When neural progenitor cells were subjected to various mitochondrial stress drugs or mitoAβ expression, we observed that KDM5A was degraded by the ubiquitin-proteasome system. It is worth noting that mitochondria dysfunction may contribute to regulating the degradation of epigenetic regulators for AHN. Both Aβ accumulation in mitochondria and indirect mitochondrial damage caused through various signaling pathways in the AD environment can lead to degradation of KDM5A, resulting in AHN deficits. Our study further investigates KDM5A may be involved in the transcriptional regulation of genes important for neurogenesis and morphogenesis in differentiating cells. During the differentiation of neural progenitor cells, KDM5A was found to promote transcription of *BDNF* and *MEF2A*, which are required for AHN. Also, we find that pharmacological and genetic reduction of KDM5A inhibited neural differentiation and cause memory deficits.

Conclusion

We herein report that mitochondrial damage in neural progenitor cells inhibits their differentiation into mature neurons. Moreover, mitochondrial dysfunction promotes the degradation of the epigenetic regulator, KDM5A, which regulates neuronal differentiation, leading to AHN deficits. Our results together imply that restoration of mitochondrial function in the hippocampal niche of AD brains may protect against the AHN declines caused by AD pathogenesis, and this may suggest new approaches for the treatment of AD.

List Of Abbreviations

AD, Alzheimer's disease

Aβ, Amyloid beta

MitoAβ, mitochondria-targeted Aβ

FAD, Familial alzheimer's disease

KDM5A, Lysine demethylase 5A

AHN, Adult hippocampal neurogenesis

SVZ, Subventricular zone

SGZ, Subgranular zone

DCX, Doublecortin

NSC, Neural stem cell

SMF, Superficial mossy fiber

IMF, Infrapyramidal mossy fiber

CaMKII, Ca^{2+}/calmodulin-dependent protein kinase II

AMPK, AMP-activated protein kinase

OGT, O-linked N-acetylglucosamine transferase

Declarations

Ethics approval and consent to participate

Animals were treated and maintained as per the Helsinki Treaty, the Principles of Laboratory Animal Care (NIH publication No. 85–23, revised 1985), and the Animal Care and Use Guidelines of Seoul National

University, Seoul, Korea. All experimental procedures were reviewed and approved by the Institutional Animal Care and Use Committee (IACUC) of Seoul National University.

Consent for publication

Not applicable

Availability of data and material

All data generated or analyzed during this study are included in this published article and its supplementary information files.

Competing interests

The authors declare that they have no competing interests.

Funding

This work was supported by the National Research Foundation of Korea (NRF) Grant funded by the Korean Government (MSIP) (NRF-2018R1A5A2025964 and 2018R1A2A1A19019062) to I. Mook-Jung. This work was also supported in part by a grant of the Collaborative Genome Program for Fostering New Post-Genome Industry (NRF-2017M3C9A5031597) to S.-W. Lee.

Author contributions

D.K.K., M-Y.C., and K.S. performed and analyzed the *in vivo* experiments. D.K.K., S.H., S.J.H., H.R., M-S.C., and Y-S.K. performed and analyzed the *in vitro* experiments. M.K. and Y-S.K. produced lentivirus for mitoAβ transduction. J.B., H.K., and S-W.L performed proteomic analysis. H.J. and D.H. performed bioinformatics analysis. D.S. and J-I.K. analyzed ChIP-seq database. D.K.K. and I.M-J planned the study and D.K.K., S-W.L., D.H., and I.M-J. wrote the manuscript. All authors have read and approved the final manuscript.

References

1. Kempermann G, Song H, Gage FH: **Neurogenesis in the Adult Hippocampus.** *Cold Spring Harb Perspect Biol* 2015, **7:**a018812.
2. Ming GL, Song H: **Adult neurogenesis in the mammalian brain: significant answers and significant questions.** *Neuron* 2011, **70:**687-702.
3. Gage FH: **Adult neurogenesis in mammals.** *Science* 2019, **364:**827-828.
4. von Bohlen Und Halbach O: **Immunohistological markers for staging neurogenesis in adult hippocampus.** *Cell Tissue Res* 2007, **329:**409-420.
5. Moreno-Jimenez EP, Flor-Garcia M, Terreros-Roncal J, Rabano A, Cafini F, Pallas-Bazarra N, Avila J, Llorens-Martin M: **Adult hippocampal neurogenesis is abundant in neurologically healthy subjects**

and drops sharply in patients with Alzheimer's disease. *Nat Med* 2019, **25:**554-560.

6. Choi SH, Bylykbashi E, Chatila ZK, Lee SW, Pulli B, Clemenson GD, Kim E, Rompala A, Oram MK, Asselin C, et al: **Combined adult neurogenesis and BDNF mimic exercise effects on cognition in an Alzheimer's mouse model.** *Science* 2018, **361**.
7. Demars M, Hu YS, Gadadhar A, Lazarov O: **Impaired neurogenesis is an early event in the etiology of familial Alzheimer's disease in transgenic mice.** *J Neurosci Res* 2010, **88:**2103-2117.
8. Rodriguez JJ, Jones VC, Tabuchi M, Allan SM, Knight EM, LaFerla FM, Oddo S, Verkhratsky A: **Impaired adult neurogenesis in the dentate gyrus of a triple transgenic mouse model of Alzheimer's disease.** *PLoS One* 2008, **3:**e2935.
9. Folmes CD, Nelson TJ, Martinez-Fernandez A, Arrell DK, Lindor JZ, Dzeja PP, Ikeda Y, Perez-Terzic C, Terzic A: **Somatic oxidative bioenergetics transitions into pluripotency-dependent glycolysis to facilitate nuclear reprogramming.** *Cell Metab* 2011, **14:**264-271.
10. Khacho M, Harris R, Slack RS: **Mitochondria as central regulators of neural stem cell fate and cognitive function.** *Nat Rev Neurosci* 2019, **20:**34-48.
11. Khacho M, Clark A, Svoboda DS, Azzi J, MacLaurin JG, Meghaizel C, Sesaki H, Lagace DC, Germain M, Harper ME, et al: **Mitochondrial Dynamics Impacts Stem Cell Identity and Fate Decisions by Regulating a Nuclear Transcriptional Program.** *Cell Stem Cell* 2016, **19:**232-247.
12. Zhang H, Ryu D, Wu Y, Gariani K, Wang X, Luan P, D'Amico D, Ropelle ER, Lutolf MP, Aebersold R, et al: **NAD(+) repletion improves mitochondrial and stem cell function and enhances life span in mice.** *Science* 2016, **352:**1436-1443.
13. Beckervordersandforth R, Ebert B, Schaffner I, Moss J, Fiebig C, Shin J, Moore DL, Ghosh L, Trinchero MF, Stockburger C, et al: **Role of Mitochondrial Metabolism in the Control of Early Lineage Progression and Aging Phenotypes in Adult Hippocampal Neurogenesis.** *Neuron* 2017, **93:**560-573 e566.
14. Liu Z, Butow RA: **Mitochondrial retrograde signaling.** *Annu Rev Genet* 2006, **40:**159-185.
15. Kim KH, Son JM, Benayoun BA, Lee C: **The Mitochondrial-Encoded Peptide MOTS-c Translocates to the Nucleus to Regulate Nuclear Gene Expression in Response to Metabolic Stress.** *Cell Metab* 2018, **28:**516-524 e517.
16. Cha MY, Kim DK, Mook-Jung I: **The role of mitochondrial DNA mutation on neurodegenerative diseases.** *Exp Mol Med* 2015, **47:**e150.
17. Sidler C, Kovalchuk O, Kovalchuk I: **Epigenetic Regulation of Cellular Senescence and Aging.** *Front Genet* 2017, **8:**138.
18. Zou C, Mallampalli RK: **Regulation of histone modifying enzymes by the ubiquitin-proteasome system.** *Biochim Biophys Acta* 2014, **1843:**694-702.
19. Yu SW, Baek SH, Brennan RT, Bradley CJ, Park SK, Lee YS, Jun EJ, Lookingland KJ, Kim EK, Lee H, et al: **Autophagic death of adult hippocampal neural stem cells following insulin withdrawal.** *Stem Cells* 2008, **26:**2602-2610.

20. Ha S, Jeong SH, Yi K, Chu JJ, Kim S, Kim EK, Yu SW: **Autophagy Mediates Astrogenesis in Adult Hippocampal Neural Stem Cells.** *Exp Neurobiol* 2019, **28:**229-246.
21. Wisniewski JR, Zougman A, Nagaraj N, Mann M: **Universal sample preparation method for proteome analysis.** *Nat Methods* 2009, **6:**359-362.
22. Park JM, Park JH, Mun DG, Bae J, Jung JH, Back S, Lee H, Kim H, Jung HJ, Kim HK, et al: **Integrated analysis of global proteome, phosphoproteome, and glycoproteome enables complementary interpretation of disease-related protein networks.** *Sci Rep* 2015, **5:**18189.
23. Lee H, Mun DG, Bae J, Kim H, Oh SY, Park YS, Lee JH, Lee SW: **A simple dual online ultra-high pressure liquid chromatography system (sDO-UHPLC) for high throughput proteome analysis.** *Analyst* 2015, **140:**5700-5706.
24. Hyung SW, Kim MS, Mun DG, Lee H, Lee SW: **The effect and potential of using a temperature controlled separation column with ultra-high pressure microcapillary liquid chromatography/tandem mass spectrometry on proteomic analysis.** *Analyst* 2011, **136:**2100-2105.
25. Shin B, Jung HJ, Hyung SW, Kim H, Lee D, Lee C, Yu MH, Lee SW: **Postexperiment monoisotopic mass filtering and refinement (PE-MMR) of tandem mass spectrometric data increases accuracy of peptide identification in LC/MS/MS.** *Mol Cell Proteomics* 2008, **7:**1124-1134.
26. Kim S, Mischerikow N, Bandeira N, Navarro JD, Wich L, Mohammed S, Heck AJ, Pevzner PA: **The generating function of CID, ETD, and CID/ETD pairs of tandem mass spectra: applications to database search.** *Mol Cell Proteomics* 2010, **9:**2840-2852.
27. Madar IH, Back S, Mun DG, Kim H, Jung JH, Kim KP, Lee SW: **Reduction of Ambiguity in Phosphorylation-site Localization in Large-scale Phosphopeptide Profiling by Data Filter using Unique Mass Class Information.** *B Korean Chem Soc* 2014, **35:**845-850.
28. Zhang B, Chambers MC, Tabb DL: **Proteomic parsimony through bipartite graph analysis improves accuracy and transparency.** *J Proteome Res* 2007, **6:**3549-3557.
29. Bolstad BM, Irizarry RA, Astrand M, Speed TP: **A comparison of normalization methods for high density oligonucleotide array data based on variance and bias.** *Bioinformatics* 2003, **19:**185-193.
30. Chae S, Ahn BY, Byun K, Cho YM, Yu MH, Lee B, Hwang D, Park KS: **A systems approach for decoding mitochondrial retrograde signaling pathways.** *Sci Signal* 2013, **6:**rs4.
31. Huang da W, Sherman BT, Lempicki RA: **Systematic and integrative analysis of large gene lists using DAVID bioinformatics resources.** *Nat Protoc* 2009, **4:**44-57.
32. Herrup K, Yang Y: **Cell cycle regulation in the postmitotic neuron: oxymoron or new biology?** *Nat Rev Neurosci* 2007, **8:**368-378.
33. Singec I, Knoth R, Ditter M, Hagemeyer CE, Rosenbrock H, Frotscher M, Volk B: **Synaptic vesicle protein synaptoporin is differently expressed by subpopulations of mouse hippocampal neurons.** *J Comp Neurol* 2002, **452:**139-153.
34. Oakley H, Cole SL, Logan S, Maus E, Shao P, Craft J, Guillozet-Bongaarts A, Ohno M, Disterhoft J, Van Eldik L, et al: **Intraneuronal beta-amyloid aggregates, neurodegeneration, and neuron loss in**

transgenic mice with five familial Alzheimer's disease mutations: potential factors in amyloid plaque formation. *J Neurosci* 2006, **26:**10129-10140.

35. Beccari S, Valero J, Maletic-Savatic M, Sierra A: **A simulation model of neuroprogenitor proliferation dynamics predicts age-related loss of hippocampal neurogenesis but not astrogenesis.** *Sci Rep* 2017, **7:**16528.
36. Ernst A, Frisen J: **Adult neurogenesis in humans- common and unique traits in mammals.** *PLoS Biol* 2015, **13:**e1002045.
37. Cha MY, Han SH, Son SM, Hong HS, Choi YJ, Byun J, Mook-Jung I: **Mitochondria-specific accumulation of amyloid beta induces mitochondrial dysfunction leading to apoptotic cell death.** *PLoS One* 2012, **7:**e34929.
38. Lu C, Thompson CB: **Metabolic regulation of epigenetics.** *Cell Metab* 2012, **16:**9-17.
39. Tsukada Y, Fang J, Erdjument-Bromage H, Warren ME, Borchers CH, Tempst P, Zhang Y: **Histone demethylation by a family of JmjC domain-containing proteins.** *Nature* 2006, **439:**811-816.
40. Dehennaut V, Leprince D, Lefebvre T: **O-GlcNAcylation, an Epigenetic Mark. Focus on the Histone Code, TET Family Proteins, and Polycomb Group Proteins.** *Front Endocrinol (Lausanne)* 2014, **5:**155.
41. Bungard D, Fuerth BJ, Zeng PY, Faubert B, Maas NL, Viollet B, Carling D, Thompson CB, Jones RG, Berger SL: **Signaling kinase AMPK activates stress-promoted transcription via histone H2B phosphorylation.** *Science* 2010, **329:**1201-1205.
42. Casley CS, Canevari L, Land JM, Clark JB, Sharpe MA: **Beta-amyloid inhibits integrated mitochondrial respiration and key enzyme activities.** *J Neurochem* 2002, **80:**91-100.
43. Gibson GE, Zhang H, Sheu KF, Bogdanovich N, Lindsay JG, Lannfelt L, Vestling M, Cowburn RF: **Alpha-ketoglutarate dehydrogenase in Alzheimer brains bearing the APP670/671 mutation.** *Ann Neurol* 1998, **44:**676-681.
44. Giorgi C, Marchi S, Pinton P: **The machineries, regulation and cellular functions of mitochondrial calcium.** *Nat Rev Mol Cell Biol* 2018, **19:**713-730.
45. Spalding KL, Bergmann O, Alkass K, Bernard S, Salehpour M, Huttner HB, Bostrom E, Westerlund I, Vial C, Buchholz BA, et al: **Dynamics of hippocampal neurogenesis in adult humans.** *Cell* 2013, **153:**1219-1227.
46. Moon M, Cha MY, Mook-Jung I: **Impaired hippocampal neurogenesis and its enhancement with ghrelin in 5XFAD mice.** *J Alzheimers Dis* 2014, **41:**233-241.

Figures

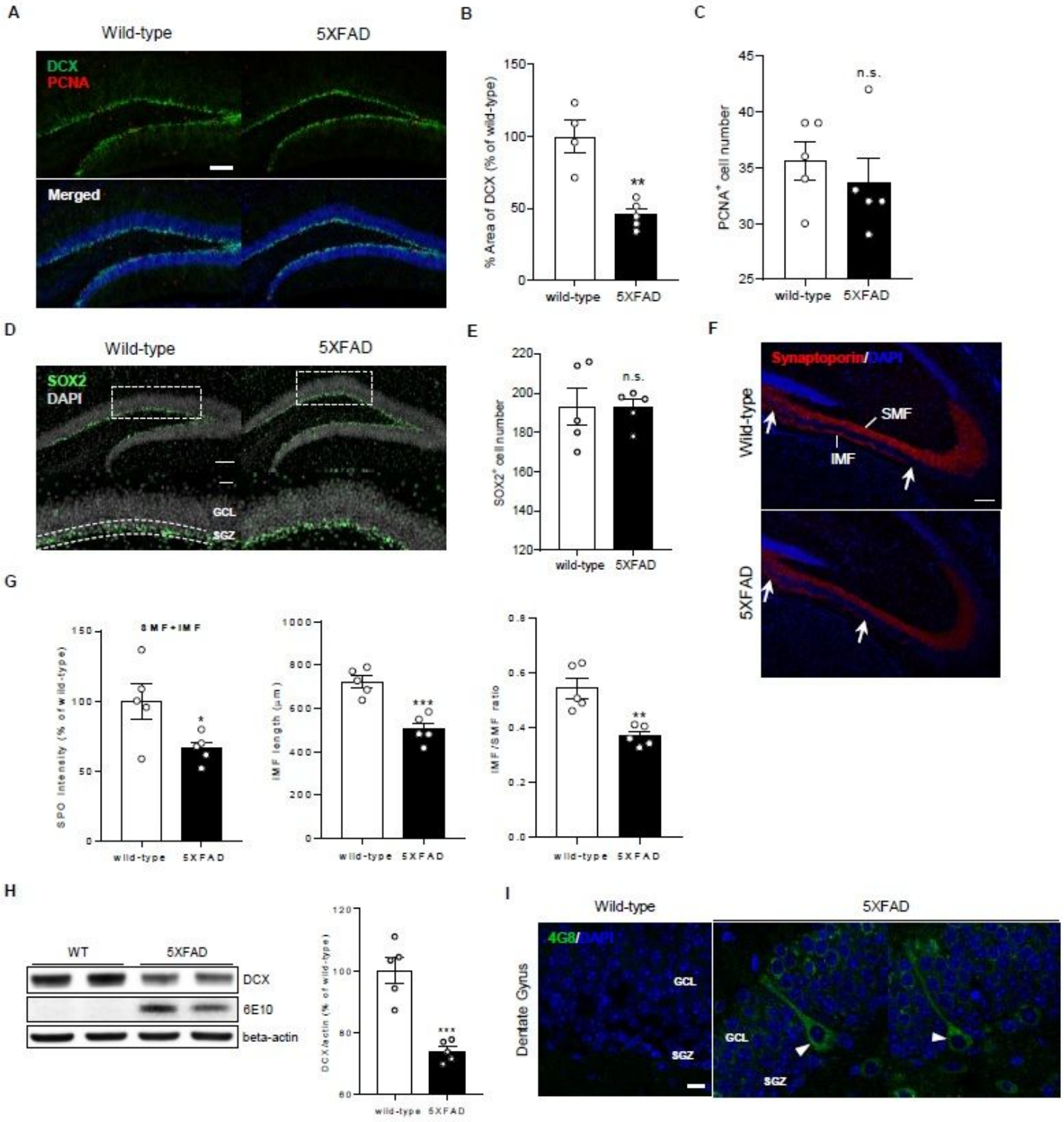

Figure 1

Inhibition of neuronal differentiation and AHN deficits in 6-week-old 5XFAD Mice (A) Immunostaining of DCX and PCNA in the DG of wild-type and 5XFAD mice. Scale bar, 100 μm. (B) Quantitative analysis of DCX intensities in the DG of wild-type and 5XFAD mice. Unpaired t-test, n = 4 (wild-type) or 5 (5XFAD) mice. (C) Quantitative analysis of the number of PCNA+ cells in the DG of wild-type and 5XFAD mice. Unpaired t-test, n = 5 mice in each group. (D) Immunostaining of SOX2 in the DG of wild-type and 5XFAD

mice. Scale bar, 100 μm. The enlarged image showing SOX2 staining in the SGZ. Scale bar, 100 μm. (E) Quantitative analysis of the number of SOX2+ cells in the SGZ of wild-type and 5XFAD mice. Unpaired t-test, n = 5 mice in each group. (F) Immunostaining of synaptoporin in the hippocampus of wild-type and 5XFAD mice. Arrows indicates the beginning and end of the IMF. SMF: superficial mossy fiber, IMF: Infrapyramidal mossy fiber. Scale bar, 100 μm. (G) Quantitative analysis of synaptoporin intensities for both SMF and IMF, IMF length, and IMF/SMF ratio in wild-type and 5XFAD mice. Unpaired t-test, n = 5 mice in each group. (H) Reduced DCX levels and presence of Aβ confirmed by western blot analysis in the hippocampus of wild-type and 5XFAD mice. Unpaired t-test, n = 5 mice in each group. (I) A representative image showing the presence of Aβ in the SGZ of wild-type and 5XFAD mice. Arrow heads indicate intraneuronal accumulation of Aβ in granule cells. SGZ: Subgranule zone, GCL: Granule cell layer. Scale bar, 10 μm. All results are represented as mean ± SEM. * $P < 0.05$; ** $P < 0.01$; *** $P < 0.001$.

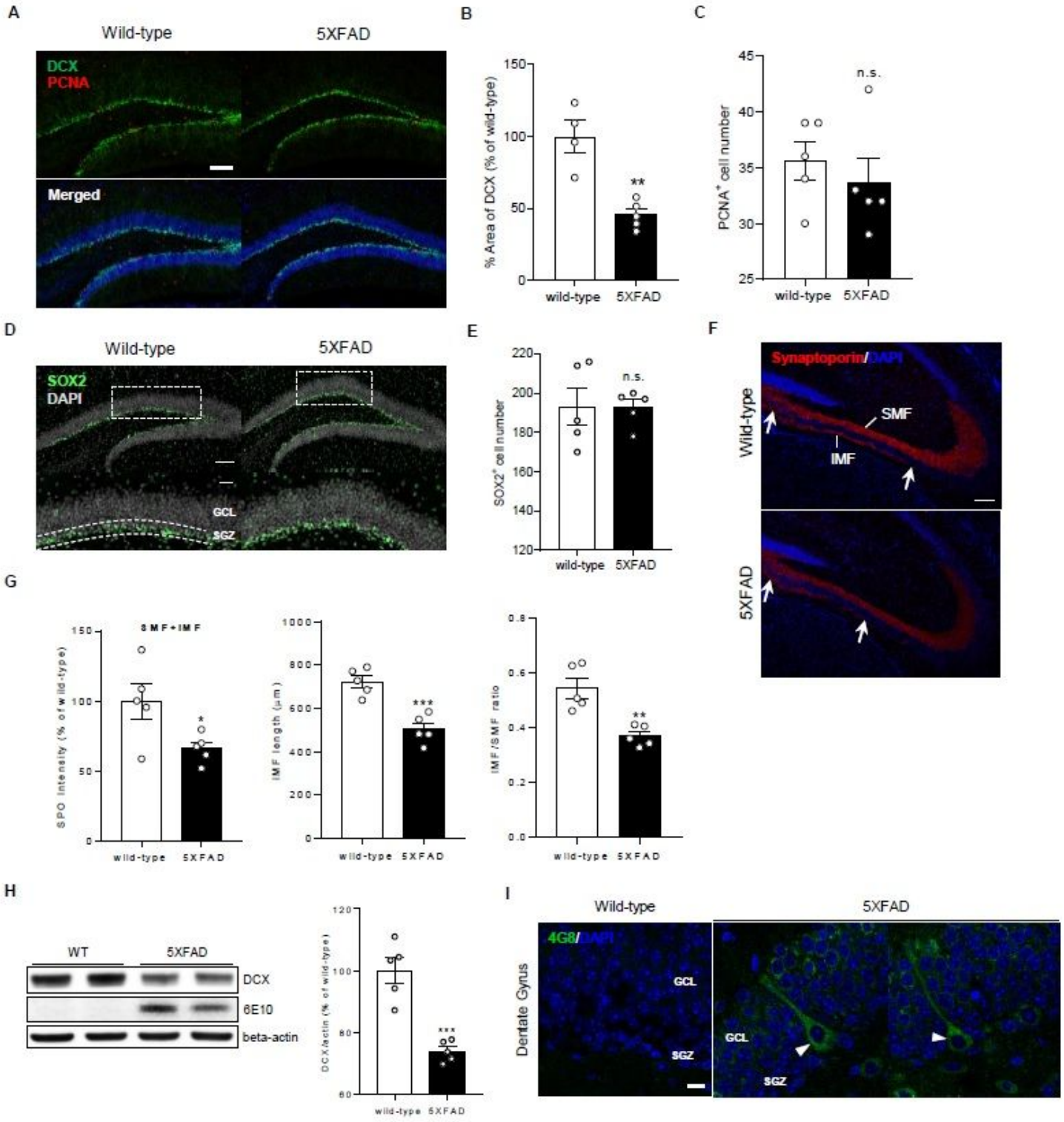

Figure 1

Inhibition of neuronal differentiation and AHN deficits in 6-week-old 5XFAD Mice (A) Immunostaining of DCX and PCNA in the DG of wild-type and 5XFAD mice. Scale bar, 100 μm. (B) Quantitative analysis of DCX intensities in the DG of wild-type and 5XFAD mice. Unpaired t-test, n = 4 (wild-type) or 5 (5XFAD) mice. (C) Quantitative analysis of the number of PCNA+ cells in the DG of wild-type and 5XFAD mice. Unpaired t-test, n = 5 mice in each group. (D) Immunostaining of SOX2 in the DG of wild-type and 5XFAD

mice. Scale bar, 100 μm. The enlarged image showing SOX2 staining in the SGZ. Scale bar, 100 μm. (E) Quantitative analysis of the number of SOX2+ cells in the SGZ of wild-type and 5XFAD mice. Unpaired t-test, n = 5 mice in each group. (F) Immunostaining of synaptoporin in the hippocampus of wild-type and 5XFAD mice. Arrows indicates the beginning and end of the IMF. SMF: superficial mossy fiber, IMF: Infrapyramidal mossy fiber. Scale bar, 100 μm. (G) Quantitative analysis of synaptoporin intensities for both SMF and IMF, IMF length, and IMF/SMF ratio in wild-type and 5XFAD mice. Unpaired t-test, n = 5 mice in each group. (H) Reduced DCX levels and presence of Aβ confirmed by western blot analysis in the hippocampus of wild-type and 5XFAD mice. Unpaired t-test, n = 5 mice in each group. (I) A representative image showing the presence of Aβ in the SGZ of wild-type and 5XFAD mice. Arrow heads indicate intraneuronal accumulation of Aβ in granule cells. SGZ: Subgranule zone, GCL: Granule cell layer. Scale bar, 10 μm. All results are represented as mean ± SEM. * P < 0.05; ** P < 0.01; *** P < 0.001.

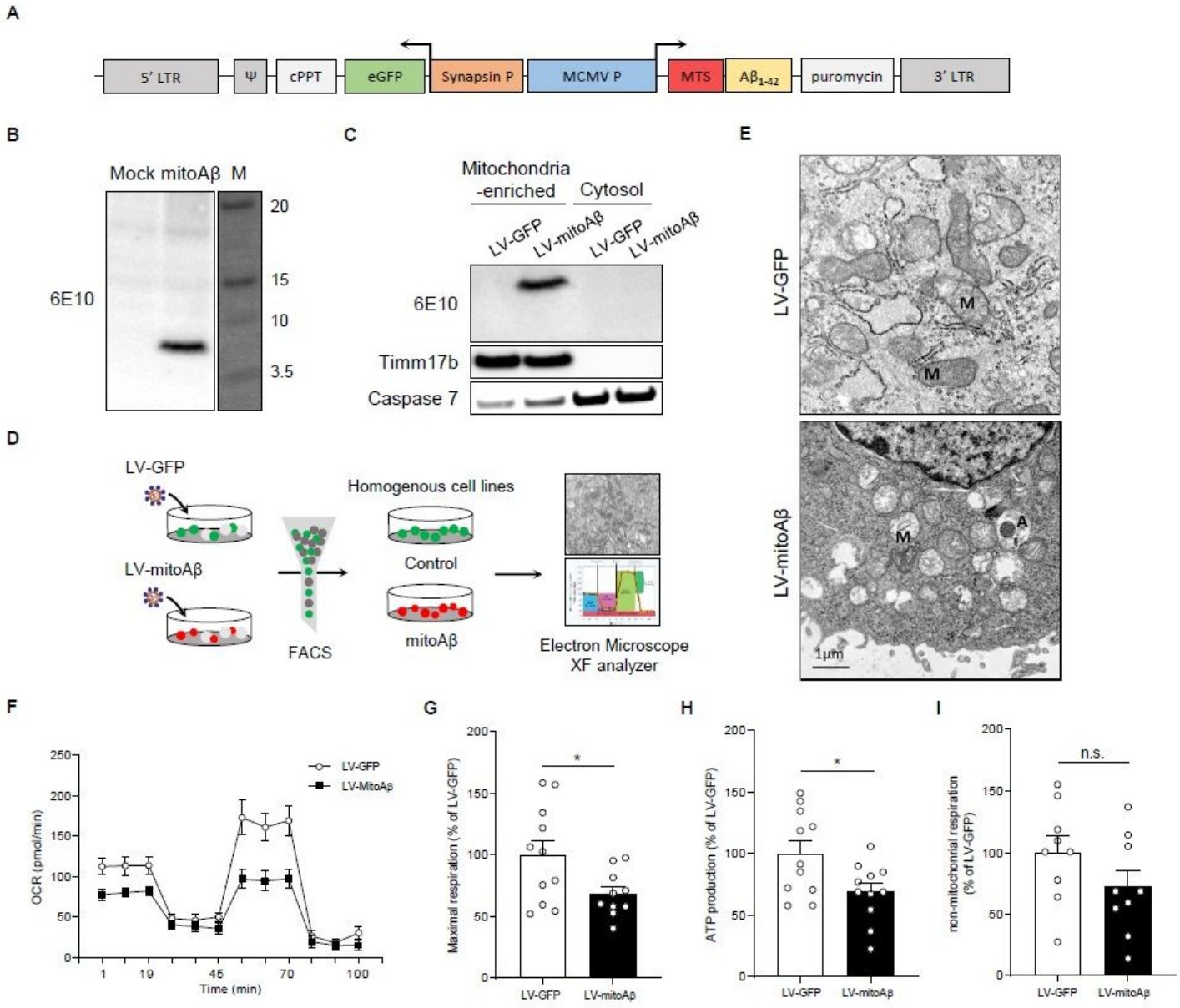

Figure 2

Mitochondria-targeted Aβ disrupts mitochondrial morphology and function (A) Diagram of mitoAβ DNA construct used in the study. (B) The expression of transfected mitoAβ in CHO cells, confirmed by the western blot analysis. (C) Subcellular localization of mitoAβ transduced by a lentiviral system was confirmed by the mitochondria-enriched fractionation. Timm17b was used as a marker for mitochondria-enriched samples and caspase 7 was used as a marker for the cytoplasm. (D) Experimental procedure of making homogenous cells expressing mitoAβ. Before analyzing cellular respiration and transmission electron microscope imaging, mitoAβ was transduced into the HT22 cell line using a lentiviral system, and GFP+ or GFP/mitoAβ+ cells were collected by FACS. (E) Mitochondria in the cytoplasm of GFP+ or GFP/mitoAβ+ cells imaged by transmission electron microscopy. M: Mitochondria, A: Autophagosome. (F) Cellular respiration rate was measured by an XF analyzer. (G-I) Quantitative analysis of the maximum respiratory rate, ATP production amount, and mitochondria-independent respiratory rates of GFP+ or GFP/mitoAβ+ cells. Unpaired t-test, n = 9-11 in each group. All results are represented as mean ± SEM. * P < 0.05.

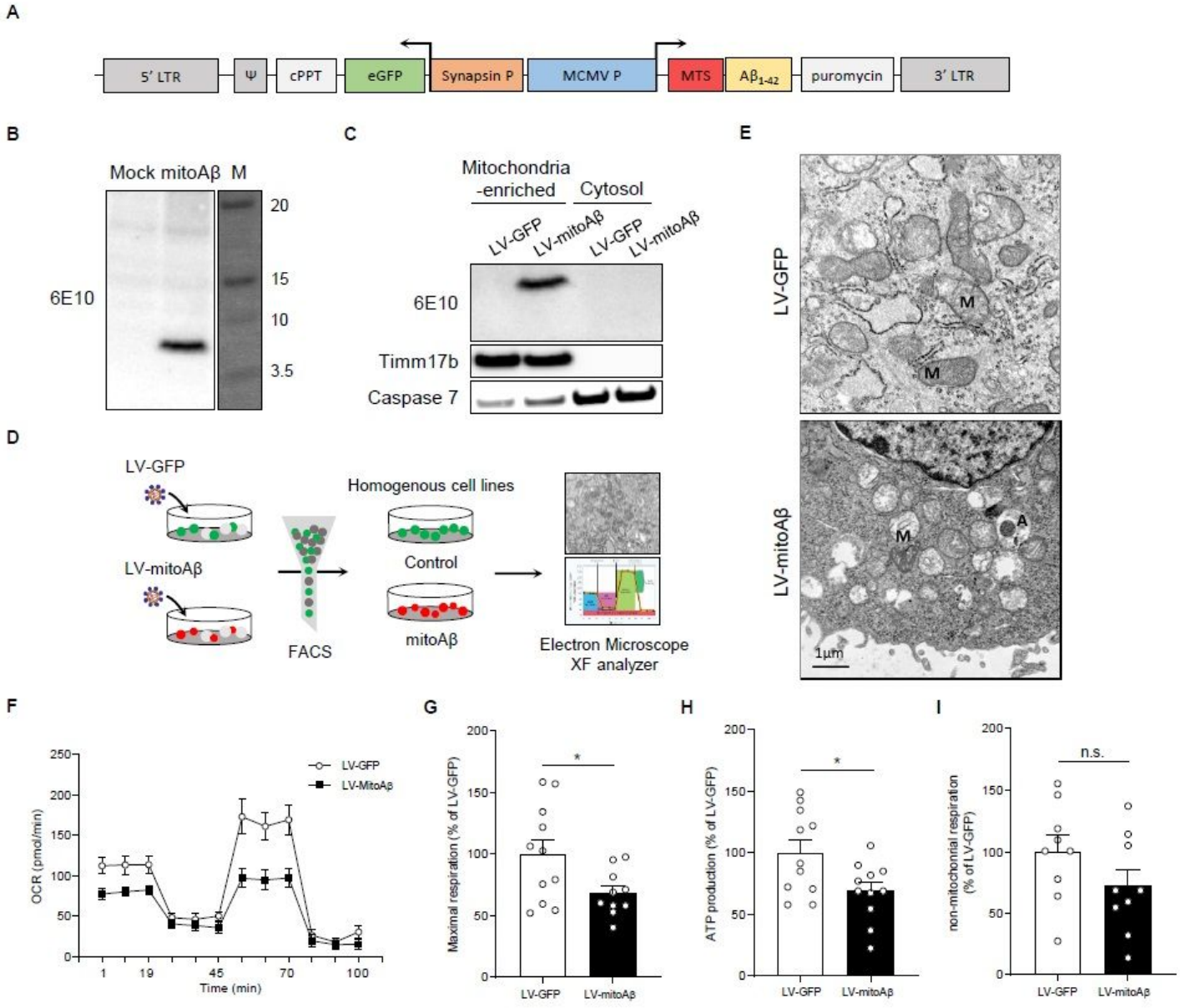

Figure 2

Mitochondria-targeted Aβ disrupts mitochondrial morphology and function (A) Diagram of mitoAβ DNA construct used in the study. (B) The expression of transfected mitoAβ in CHO cells, confirmed by the western blot analysis. (C) Subcellular localization of mitoAβ transduced by a lentiviral system was confirmed by the mitochondria-enriched fractionation. Timm17b was used as a marker for mitochondria-enriched samples and caspase 7 was used as a marker for the cytoplasm. (D) Experimental procedure of making homogenous cells expressing mitoAβ. Before analyzing cellular respiration and transmission electron microscope imaging, mitoAβ was transduced into the HT22 cell line using a lentiviral system, and GFP+ or GFP/mitoAβ+ cells were collected by FACS. (E) Mitochondria in the cytoplasm of GFP+ or GFP/mitoAβ+ cells imaged by transmission electron microscopy. M: Mitochondria, A: Autophagosome. (F) Cellular respiration rate was measured by an XF analyzer. (G-I) Quantitative analysis of the maximum respiratory rate, ATP production amount, and mitochondria-independent respiratory rates of GFP+ or GFP/mitoAβ+ cells. Unpaired t-test, n = 9-11 in each group. All results are represented as mean ± SEM. * $P < 0.05$.

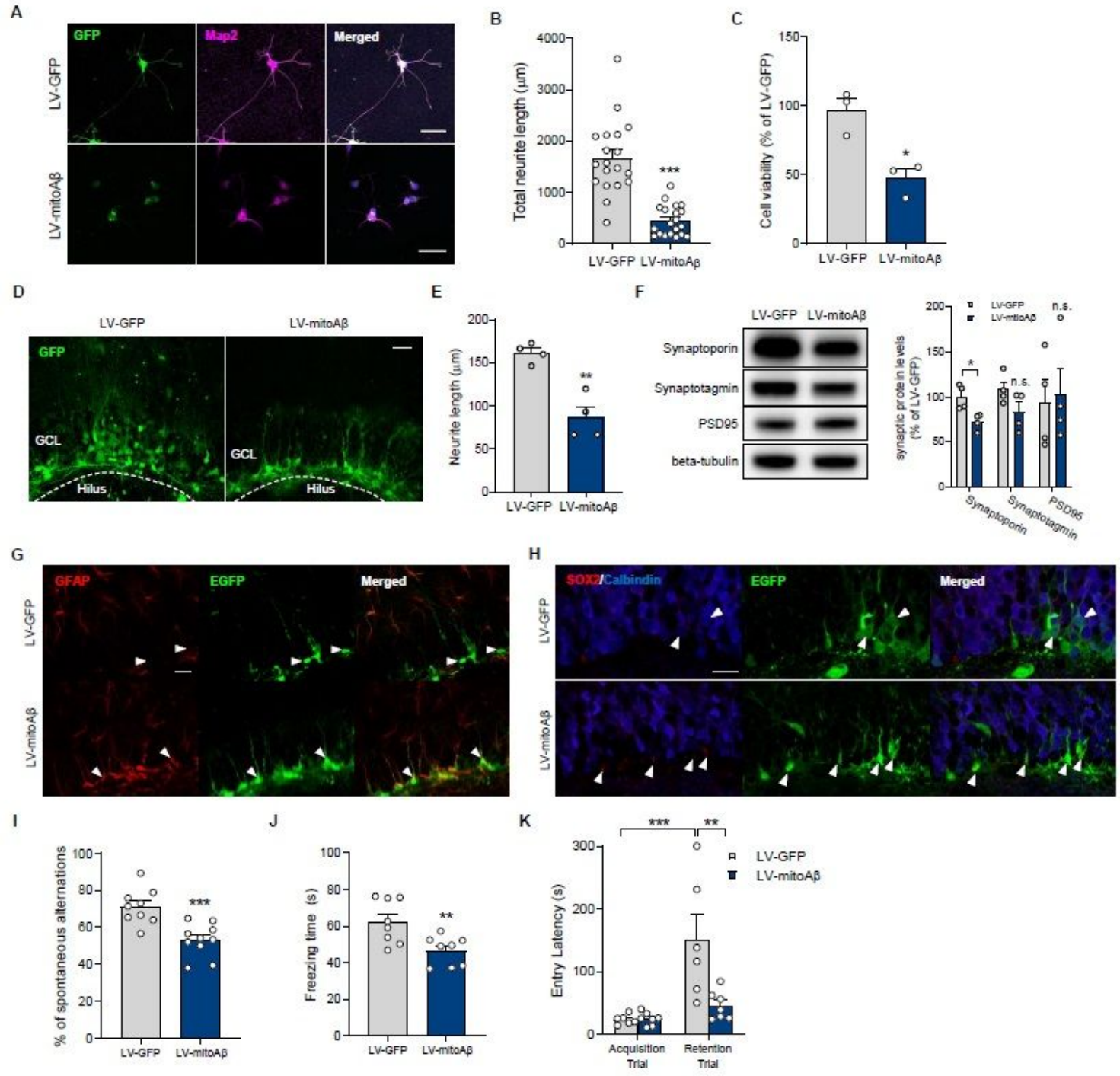

Figure 3

AHN deficits caused by mitoAβ result in cognitive impairment (A) Representative images showing that the expression of mitoAβ in adult hippocampal neural stem cells dysregulated neuronal differentiation in vitro. Scale bar, 50 μm. (B) Quantitative analysis of the neurite length of differentiated GFP+ or GFP/mitoAβ+ cells. Unpaired t-test, n = 20 neurons in each group. (C) MitoAβ expression led to the consequential reduction in cell viability. Unpaired t-test, n = 3 in each group. (D) Representative images showing that mitoAβ expression suppressed neuronal differentiation. GCL: Granule cell layer. Scale bar, 30 μm. (E) Quantitative analysis of the neurite length in the GCL of LV-GFP or LV-mitoAβ mice. Unpaired t-

test, n = 4 mice in each group. (F) Synaptoporin was specifically reduced in the hippocampus of LV-mitoAβ group, but not other synaptic proteins. Data was normalized to β-tubulin and the mean value of LV-GFP group for each protein. Unpaired t-test, n = 4 (LV-GFP) or 5 (LV-mitoAβ) mice. (G and H) GFP/mitoAβ+ cells were co-immunostained with antibodies against GFAP (G), a marker of neural stem cells, and SOX2 (H), a marker of proliferative cells, but GFP+ cells were co-immunostained with calbindin (H), a marker of mature neurons instead of GFAP and SOX2 antibodies. Scale bar, 20 μm. (I) The percentage of spontaneous alternation in Y-maze test. Unpaired t-test, n = 9 (LV-GFP) or 10 (LV-mitoAβ) mice. (J) Freezing time in CFC test. Unpaired t-test, n = 8 in each group. (K) Entry latency in PAT at acquisition and retention trial. Two-way ANOVA, n = 6 (LV-GFP) or 7 (LV-mitoAβ) mice. All results are represented as mean ± SEM. * $P < 0.05$; ** $P < 0.01$; *** $P < 0.001$.

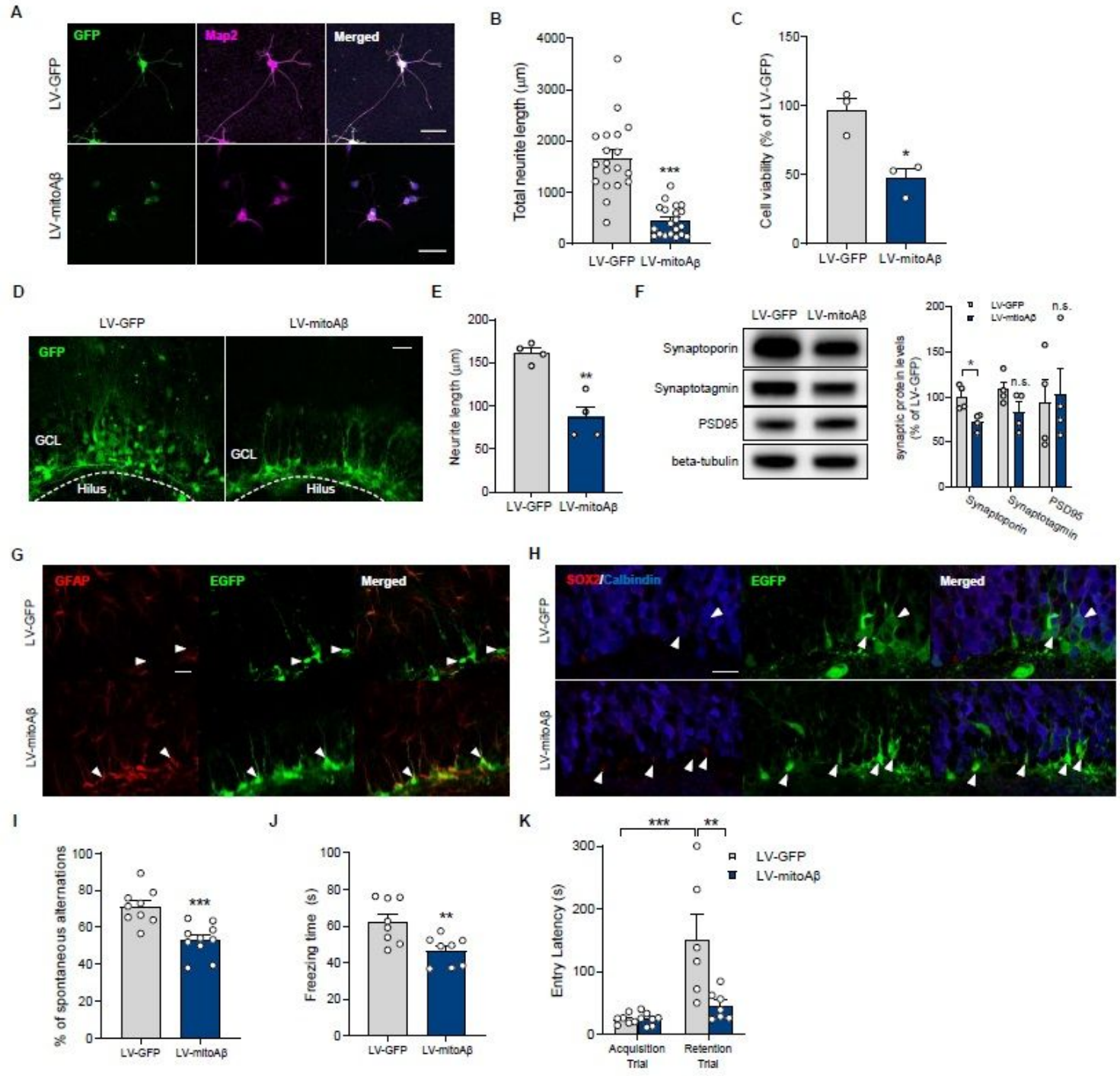

Figure 3

AHN deficits caused by mitoAβ result in cognitive impairment (A) Representative images showing that the expression of mitoAβ in adult hippocampal neural stem cells dysregulated neuronal differentiation in vitro. Scale bar, 50 μm. (B) Quantitative analysis of the neurite length of differentiated GFP+ or GFP/mitoAβ+ cells. Unpaired t-test, n = 20 neurons in each group. (C) MitoAβ expression led to the consequential reduction in cell viability. Unpaired t-test, n = 3 in each group. (D) Representative images showing that mitoAβ expression suppressed neuronal differentiation. GCL: Granule cell layer. Scale bar, 30 μm. (E) Quantitative analysis of the neurite length in the GCL of LV-GFP or LV-mitoAβ mice. Unpaired t-

test, n = 4 mice in each group. (F) Synaptoporin was specifically reduced in the hippocampus of LV-mitoAβ group, but not other synaptic proteins. Data was normalized to β-tubulin and the mean value of LV-GFP group for each protein. Unpaired t-test, n = 4 (LV-GFP) or 5 (LV-mitoAβ) mice. (G and H) GFP/mitoAβ+ cells were co-immunostained with antibodies against GFAP (G), a marker of neural stem cells, and SOX2 (H), a marker of proliferative cells, but GFP+ cells were co-immunostained with calbindin (H), a marker of mature neurons instead of GFAP and SOX2 antibodies. Scale bar, 20 μm. (I) The percentage of spontaneous alternation in Y-maze test. Unpaired t-test, n = 9 (LV-GFP) or 10 (LV-mitoAβ) mice. (J) Freezing time in CFC test. Unpaired t-test, n = 8 in each group. (K) Entry latency in PAT at acquisition and retention trial. Two-way ANOVA, n = 6 (LV-GFP) or 7 (LV-mitoAβ) mice. All results are represented as mean ± SEM. * P < 0.05; ** P < 0.01; *** P < 0.001.

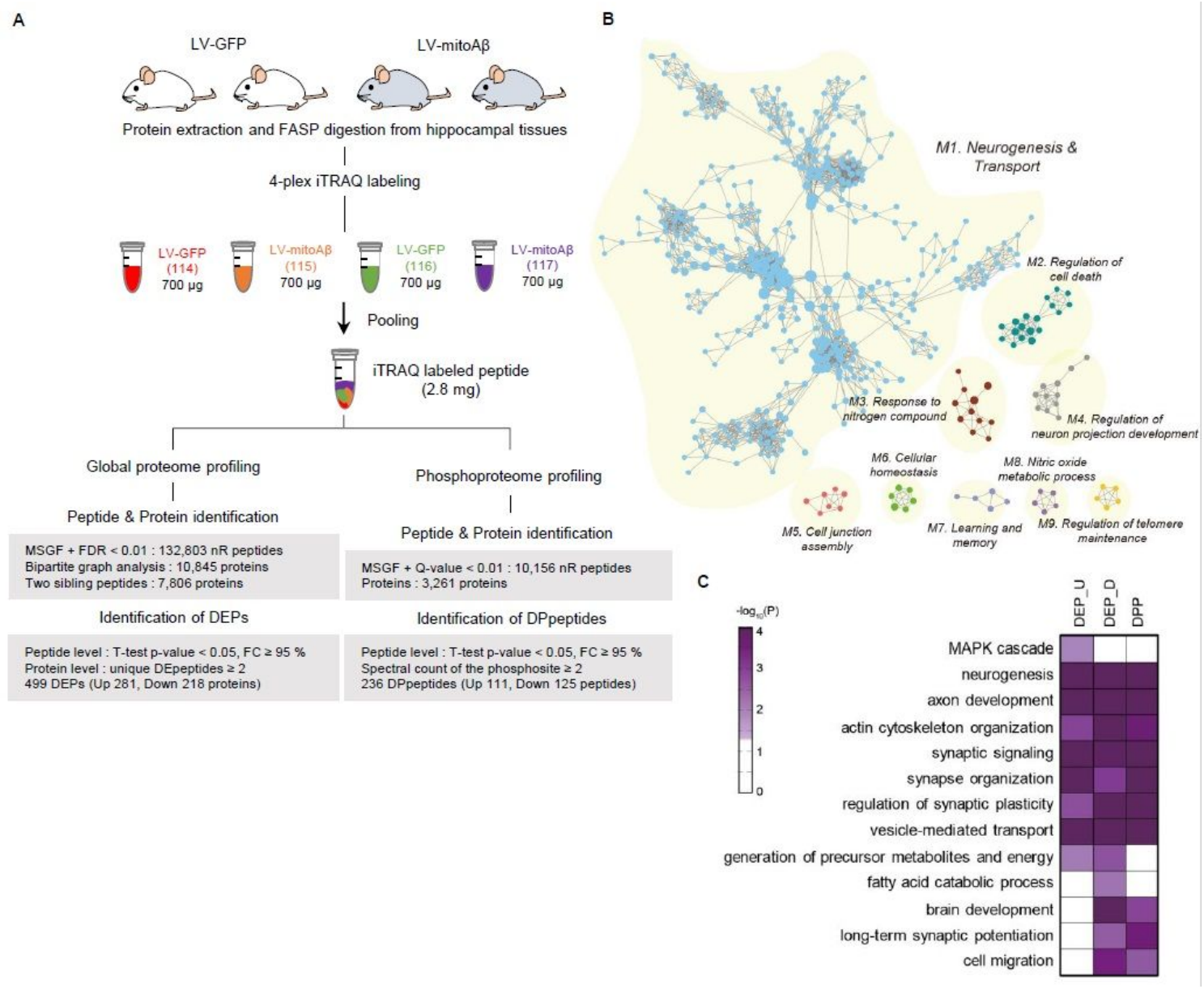

Figure 4

Proteomic and bioinformatics analyses of the hippocampus expressing mitoAβ (A) Experimental scheme and procedures of global proteome and phosphoproteome analyses of the hippocampus from two

independent LV-GFP (n=2) and LV-mitoAβ injected mice (n=2) respectively. 4-plex iTRAQ labeling followed by mRP fractionation for global proteome and phosphoproteome profilings are schematically shown. Non-redundant peptides and protein groups identified from MSGF+ search (FDR < 0.01) using global proteome and phosphoproteome data (top), as well as DEPs and DPpeptides identified by statistical testing methods (adjusted P < 0.05; bottom), are summarized in the boxes. (B) Functional modules (M1-9) of GOBPs enriched by proteins affected by mitoAβ (up- and down-regulated proteins and DPPs). In each module, the node size denotes the number of the proteins affected by mitoAβ with the corresponding GOBP, and the edge indicates that the corresponding pair of GOBPs has the significant similarity score. (C) GOBPs associated with the phenotypes altered by mitoAβ in the 'neurogenesis and transport' module. Colors in the heat map denote the significance (P-value) of GOBPs being enriched by up- (DEP_U) and down-regulated proteins (DEP_D) and DPPs. The color bar represents the gradient of –log10(P) where P is the enrichment P-value from DAVID software.

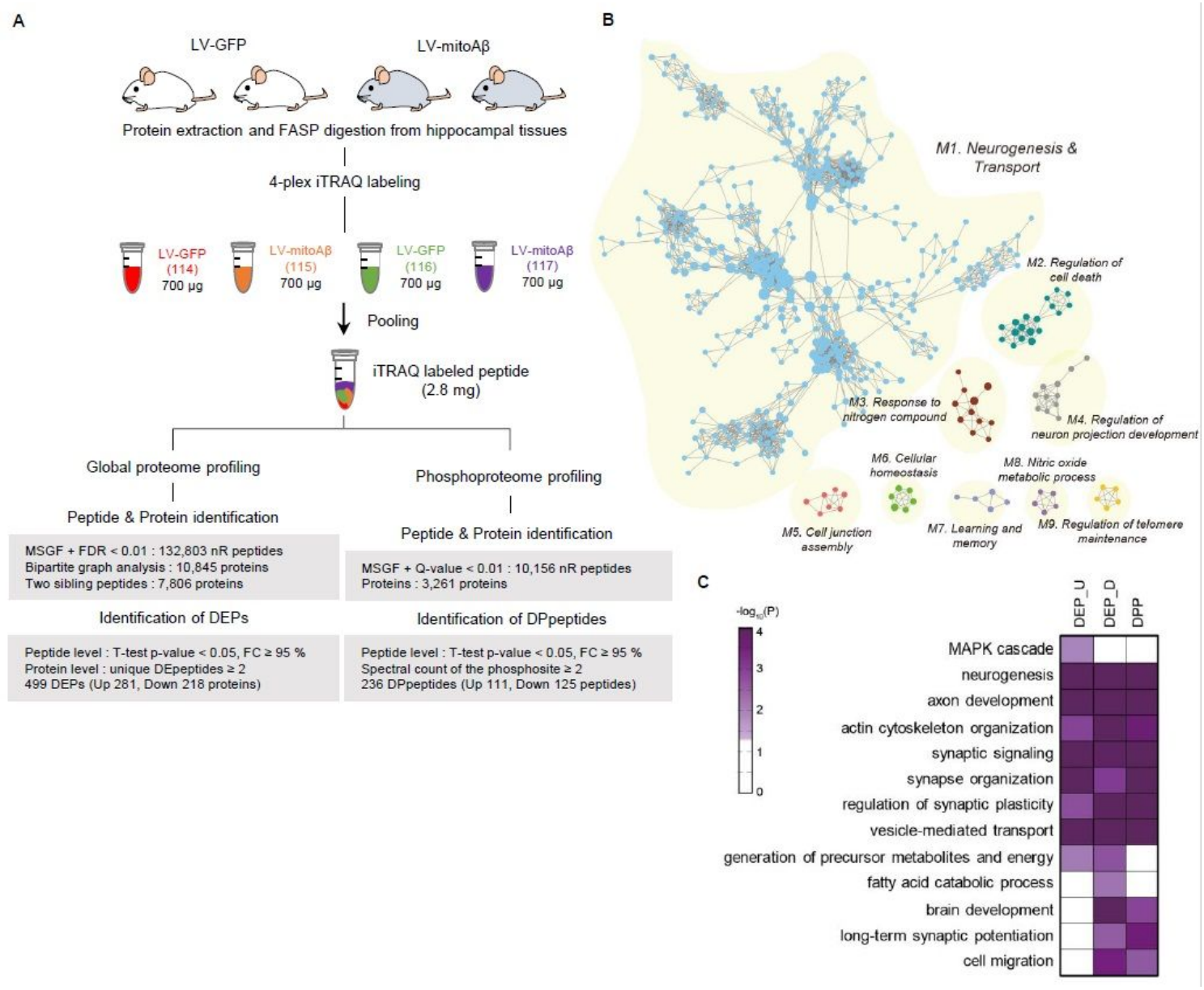

Figure 4

Proteomic and bioinformatics analyses of the hippocampus expressing mitoAβ (A) Experimental scheme and procedures of global proteome and phosphoproteome analyses of the hippocampus from two independent LV-GFP (n=2) and LV-mitoAβ injected mice (n=2) respectively. 4-plex iTRAQ labeling followed by mRP fractionation for global proteome and phosphoproteome profilings are schematically shown. Non-redundant peptides and protein groups identified from MSGF+ search (FDR < 0.01) using global proteome and phosphoproteome data (top), as well as DEPs and DPpeptides identified by statistical testing methods (adjusted P < 0.05; bottom), are summarized in the boxes. (B) Functional modules (M1-9) of GOBPs enriched by proteins affected by mitoAβ (up- and down-regulated proteins and DPPs). In each module, the node size denotes the number of the proteins affected by mitoAβ with the corresponding GOBP, and the edge indicates that the corresponding pair of GOBPs has the significant similarity score. (C) GOBPs associated with the phenotypes altered by mitoAβ in the ‘neurogenesis and transport’ module. Colors in the heat map denote the significance (P-value) of GOBPs being enriched by up- (DEP_U) and down-regulated proteins (DEP_D) and DPPs. The color bar represents the gradient of –log10(P) where P is the enrichment P-value from DAVID software.

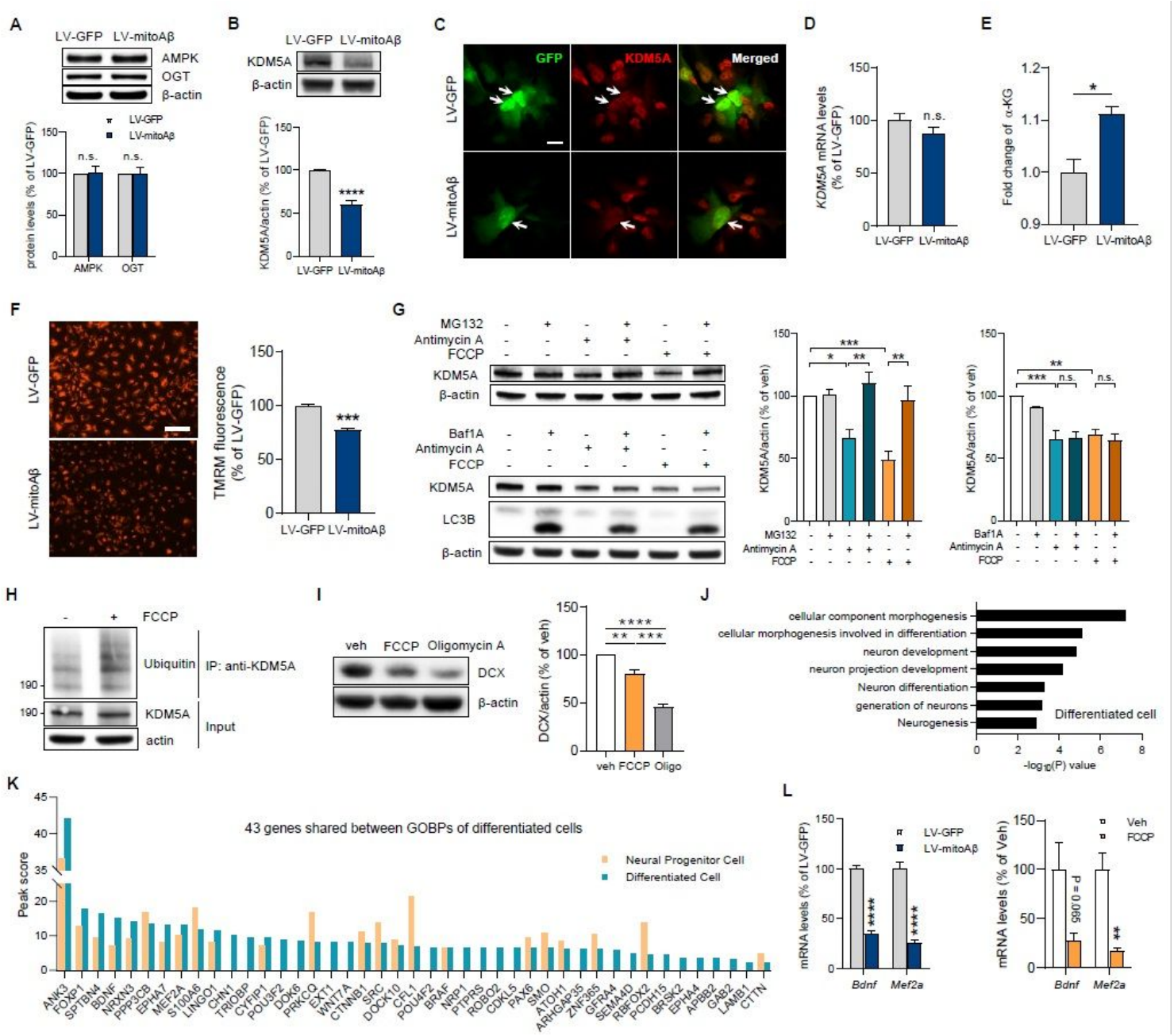

Figure 5

Mitochondrial dysfunction induces KDM5A degradation and Inhibition of neuronal differentiation in neural progenitor cells (A and B) MitoAβ expression decreased KDM5A protein levels in ReN neural progenitor cells (B), but not other epigenetic regulators, AMPK and OGT (A). Data was normalized to β-actin and the mean value of LV-GFP group for each protein. Unpaired t-test, n = 3 in each group (A) and n = 7 in each group (B). (C) Immunostaining of KDM5A in GFP+ or GFP/mitoAβ+ ReN cells. Arrows indicate lentiviral transduced cells. Scale bar, 20 μm. (D) Quantitative analysis of KDM5A mRNA levels in LV-GFP and LV-mitoAβ ReN cells. Unpaired t-test, n = 3 in each group. (E) α-KG levels quantification of LV-GFP and LV-mitoAβ ReN cells. Unpaired t-test, n = 3 in each group. (F) Representative images and quantification of mitochondrial membrane potential in LV-GFP and LV-mitoAβ ReN cells stained with TMRM dye. Scale bar, 100 μm. Unpaired t-test, n = 3 in each group. (G) Mitochondrial stress drugs

(Antimycin A and FCCP) induced to degrade KDM5A and it was restored by MG132, an inhibitor of proteasome. Bafilomycin A, an inhibitor of autophagy flux, did not rescue the degradation of KDM5A. Data was normalized to β-actin. One way-ANOVA analysis, n = 4 – 5 in each group. (H) The ubiquitination of KDM5A was increased by the treatment of FCCP. (I) DCX protein levels were reduced in differentiated cells (12 days) after treatment with FCCP (3 μM, 12 hrs) and oligomycin A (3 μM, 12 hrs) on ReN neural progenitor cells, respectively. (J) GOBPs enriched by the target genes of KDM5A in differentiated cells (5 days). The enrichment significance was shown as –log10(P) where P is the enrichment P-value. (K) Peak scores of 43 genes shared between 7 GOBPs of KDM5A-binding genes in differentiated cells in neural progenitor and differentiated cells. (L) Quantitative analysis of target genes, BDNF and MEF2A mRNA, reduced by mitoAβ and FCCP in differentiated cells (12 days). Unpaired t-test, n = 3 – 6 in each group. All results are represented as mean ± SEM. * P < 0.05; ** P < 0.01; *** P < 0.001; **** P < 0.0001.

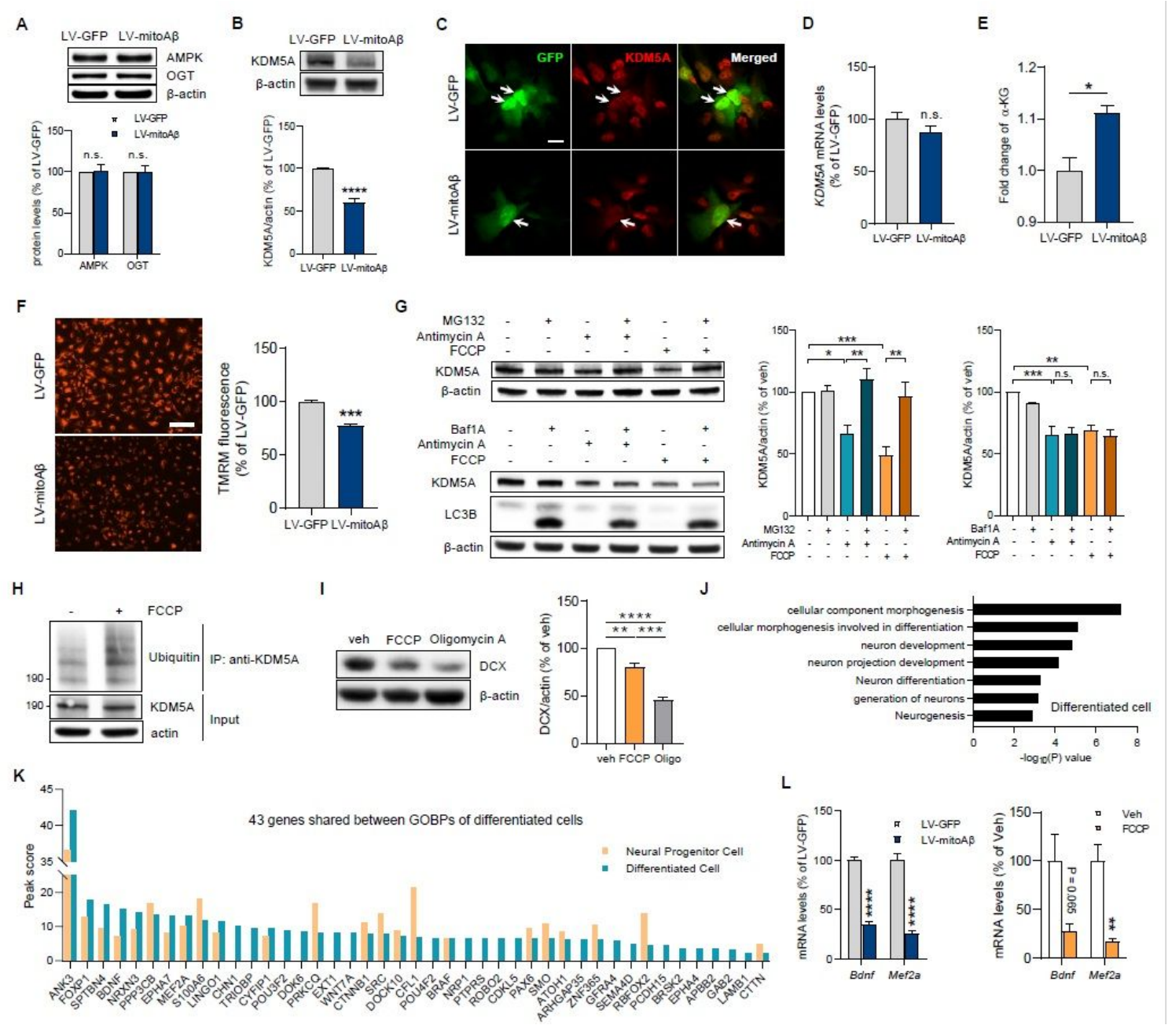

Figure 5

Mitochondrial dysfunction induces KDM5A degradation and Inhibition of neuronal differentiation in neural progenitor cells (A and B) MitoAβ expression decreased KDM5A protein levels in ReN neural progenitor cells (B), but not other epigenetic regulators, AMPK and OGT (A). Data was normalized to β-actin and the mean value of LV-GFP group for each protein. Unpaired t-test, n = 3 in each group (A) and n = 7 in each group (B). (C) Immunostaining of KDM5A in GFP+ or GFP/mitoAβ+ ReN cells. Arrows indicate lentiviral transduced cells. Scale bar, 20 μm. (D) Quantitative analysis of KDM5A mRNA levels in LV-GFP and LV-mitoAβ ReN cells. Unpaired t-test, n = 3 in each group. (E) α-KG levels quantification of LV-GFP and LV-mitoAβ ReN cells. Unpaired t-test, n = 3 in each group. (F) Representative images and quantification of mitochondrial membrane potential in LV-GFP and LV-mitoAβ ReN cells stained with TMRM dye. Scale bar, 100 μm. Unpaired t-test, n = 3 in each group. (G) Mitochondrial stress drugs (Antimycin A and FCCP) induced to degrade KDM5A and it was restored by MG132, an inhibitor of proteasome. Bafilomycin A, an inhibitor of autophagy flux, did not rescue the degradation of KDM5A. Data was normalized to β-actin. One way-ANOVA analysis, n = 4 – 5 in each group. (H) The ubiquitination of KDM5A was increased by the treatment of FCCP. (I) DCX protein levels were reduced in differentiated cells (12 days) after treatment with FCCP (3 μM, 12 hrs) and oligomycin A (3 μM, 12 hrs) on ReN neural progenitor cells, respectively. (J) GOBPs enriched by the target genes of KDM5A in differentiated cells (5 days). The enrichment significance was shown as –log10(P) where P is the enrichment P-value. (K) Peak scores of 43 genes shared between 7 GOBPs of KDM5A-binding genes in differentiated cells in neural progenitor and differentiated cells. (L) Quantitative analysis of target genes, BDNF and MEF2A mRNA, reduced by mitoAβ and FCCP in differentiated cells (12 days). Unpaired t-test, n = 3 – 6 in each group. All results are represented as mean ± SEM. * P < 0.05; ** P < 0.01; *** P < 0.001; **** P < 0.0001.

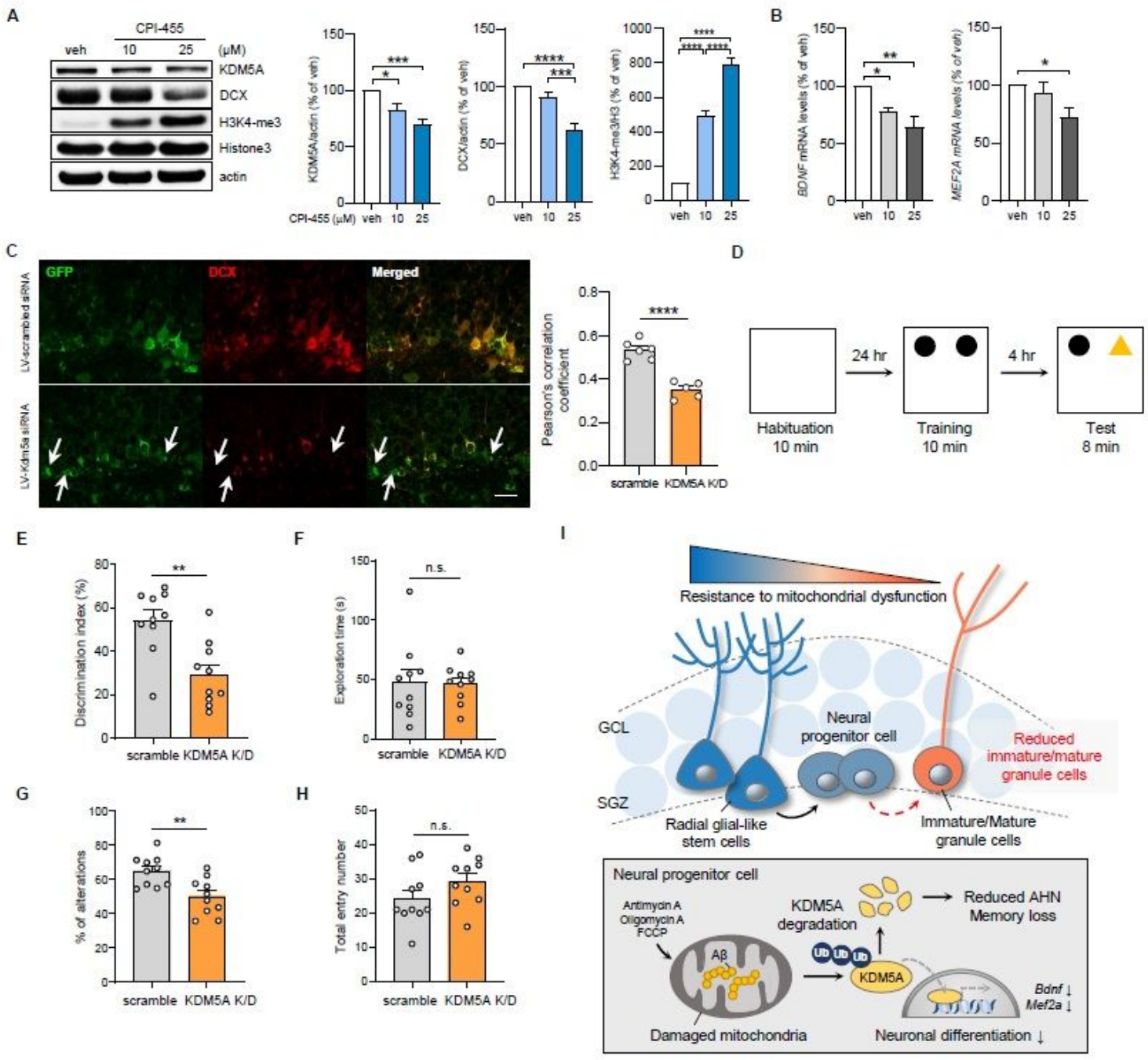

Figure 6

The inhibition or knockdown of KDM5A impairs neuronal differentiation and cognitive functions (A) An inhibitor of KDM5A, CPI-455, decreased DCX protein levels during the differentiation (12 days of differentiation). CPI-455 finally reduced KDM5A protein levels by functional inhibition and increased the amount of tri-methylated histone K3. Data were normalized to β-actin and the mean value of the vehicle group for each protein. One way-ANOVA analysis, n = 8 in each group. (B) mRNA levels of BDNF and MEF2A in differentiated cells (12 days) in which KDM5A was functionally inhibited by CPI-455. One way-ANOVA analysis, n = 6 in each group. (C) Knockdown of Kdm5a exhibited a lower correlation with DCX

expression pattern as compared to the control group. Unpaired t-test, n = 6 (scramble) or 5 (Kdm5a siRNA) mice. Scale bar, 20 μm. (D) Experimental procedure of NOR test. (E) Kdm5a knockdown mice showed a lower discrimination index to distinguish between old and new object compared to the control group. Unpaired t-test, n = 10 in each group. (F) The total exploration time of NOR test for both groups. Unpaired t-test, n = 10 in each group. (G) Kdm5a knockdown mice exhibited impaired spatial memory tested by Y-maze test. Unpaired t-test, n = 10 in each group. (H) The total entry number of Y-maze test for both groups. Unpaired t-test, n = 10 in each group. (I) Graphic summary illustrating that mitochondrial dysfunction-induced KDM5A degradation, thereby inhibiting AHN and causing cognitive impairments. All results are represented as mean ± SEM. * P < 0.05; ** P < 0.01; *** P < 0.001; **** P < 0.0001.

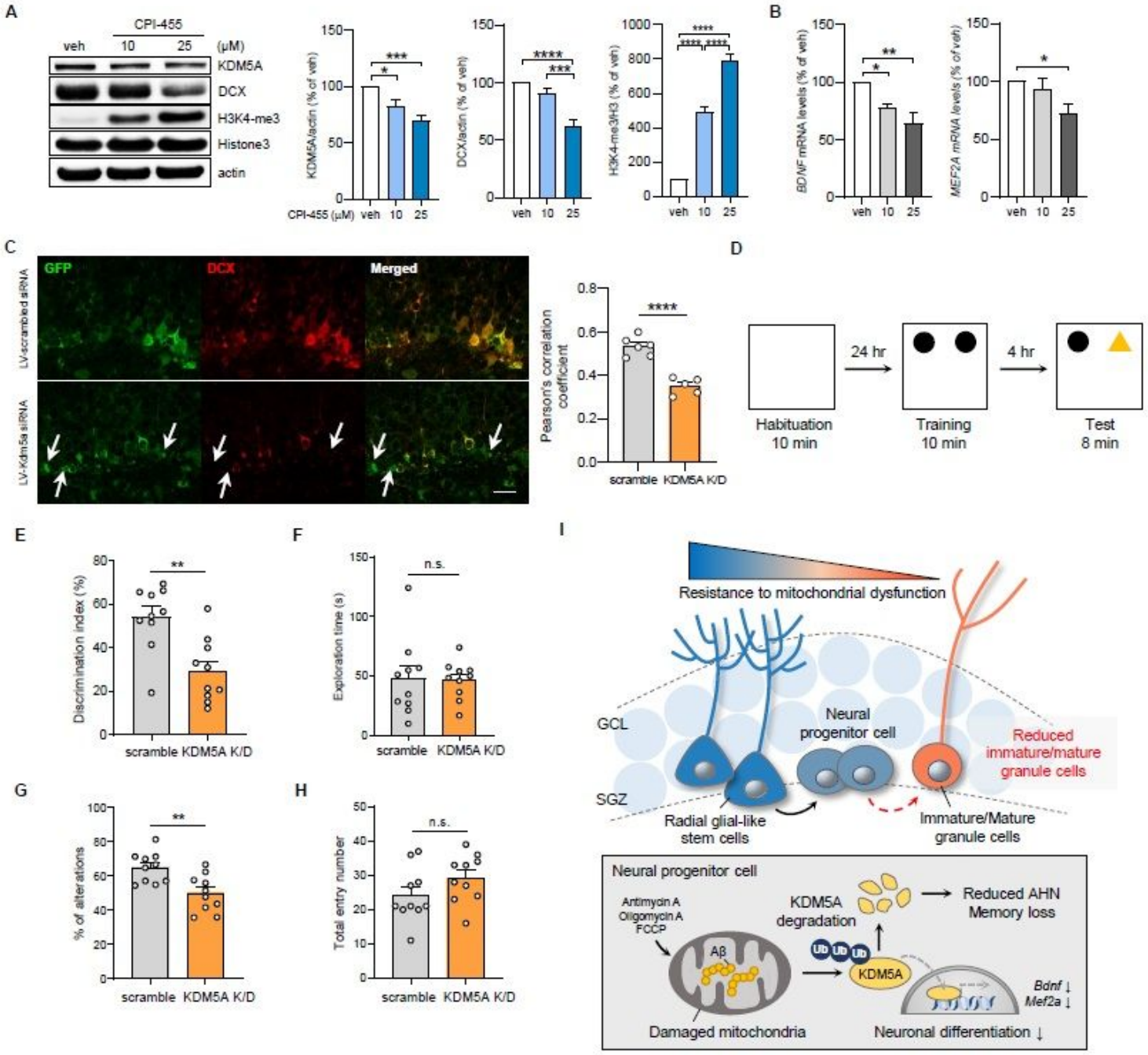

Figure 6

The inhibition or knockdown of KDM5A impairs neuronal differentiation and cognitive functions (A) An inhibitor of KDM5A, CPI-455, decreased DCX protein levels during the differentiation (12 days of differentiation). CPI-455 finally reduced KDM5A protein levels by functional inhibition and increased the amount of tri-methylated histone K3. Data were normalized to β-actin and the mean value of the vehicle group for each protein. One way-ANOVA analysis, n = 8 in each group. (B) mRNA levels of BDNF and MEF2A in differentiated cells (12 days) in which KDM5A was functionally inhibited by CPI-455. One way-ANOVA analysis, n = 6 in each group. (C) Knockdown of Kdm5a exhibited a lower correlation with DCX expression pattern as compared to the control group. Unpaired t-test, n = 6 (scramble) or 5 (Kdm5a siRNA) mice. Scale bar, 20 μm. (D) Experimental procedure of NOR test. (E) Kdm5a knockdown mice showed a lower discrimination index to distinguish between old and new object compared to the control group. Unpaired t-test, n = 10 in each group. (F) The total exploration time of NOR test for both groups. Unpaired t-test, n = 10 in each group. (G) Kdm5a knockdown mice exhibited impaired spatial memory tested by Y-maze test. Unpaired t-test, n = 10 in each group. (H) The total entry number of Y-maze test for both groups. Unpaired t-test, n = 10 in each group. (I) Graphic summary illustrating that mitochondrial dysfunction-induced KDM5A degradation, thereby inhibiting AHN and causing cognitive impairments. All results are represented as mean ± SEM. * $P < 0.05$; ** $P < 0.01$; *** $P < 0.001$; **** $P < 0.0001$.

Supplementary Files

This is a list of supplementary files associated with this preprint. Click to download.

- Additionalfile1.docx
- Additionalfile1.docx
- Additionalfile2.pdf
- Additionalfile2.pdf
- Additionalfile3.xlsx
- Additionalfile3.xlsx
- Additionalfile4.xlsb
- Additionalfile4.xlsb
- Additionalfile5.xlsx
- Additionalfile5.xlsx